J. Fluid Mech. (2002), *vol.* 463, *pp.* 259–291. © 2002 Cambridge University Press
DOI: 10.1017/S0022112002008741 Printed in the United Kingdom

Vortical flow. Part 1. Flow through a constant-diameter pipe

By T. W. MATTNER, P. N. JOUBERT AND M. S. CHONG

Department of Mechanical and Manufacturing Engineering,
University of Melbourne, Victoria 3010, Australia

(Received 27 February 2001 and in revised form 13 December 2001)

This paper describes an exploration of the behaviour and properties of swirling flow through a constant-diameter pipe. The experiments reveal a complicated transition process as the swirl intensity Ω is increased at fixed pipe Reynolds number $Re \approx 4900$. For $\Omega \leqslant 1.09$, the vortex was steady, laminar, axisymmetric, and developed slowly with streamwise distance. The upstream velocity profiles were similar to those commonly appearing in the literature in similar apparatus. Spiral vortex breakdown appeared in the test section for $1.09 \leqslant \Omega \leqslant 1.31$ and was associated with a localized transition from jet-like to wake-like mean axial velocity profiles. Further increase in Ω caused the breakdown to move upstream of the test section. Downstream, the core of the post-breakdown flow was unsteady and recovered toward jet-like profiles with streamwise distance. At $\Omega = 2.68$, a global transition occurred in which the mean axial velocity profiles suddenly developed an annular axial velocity deficit. At the same time, disturbances began to appear in the outer flow. Further increase in Ω eventually led to an annulus of reversed axial flow and a completely unsteady vortex.

1. Introduction

This paper describes various flow regimes observed in a confined vortex apparatus. The apparatus consists of a guide vane arrangement at the inlet to generate the swirl, a constant-diameter pipe through which the vortex flows, and an orifice at the outlet to control the volume flow rate. The aim is to increase our knowledge of the behaviour and properties of the vortex for a wide range of swirl intensity. This knowledge is the basis for a subsequent study of vortical flow past a sphere using the same apparatus (Mattner, Joubert & Chong 2002).

The study was motivated by the authors' observation of an extensive annular region of reverse axial flow in an apparatus similar to the one described above, except that tangential fluid injection was used to generate the swirl (Mattner, Joubert & Chong 1996; Mattner 2000). This mode of axial flow was one of three identified by Nuttal (1953) who observed a progression from unidirectional axial flow (regime I), through reversed axial flow near the axis (regime II), to an annulus of reversed axial flow (regime III) as the swirl intensity was increased. His apparatus was functionally similar to the guide vane apparatus used in this study. Other observations of regime III have been made in a variety of experimental arrangements: Binnie (1957) used fluid injection through a rotating portion of the pipe to generate the swirl while Nissan & Bresan (1961) and Guo & Dhir (1990) used tangential fluid injection at the inlet. Whereas these studies all used an impermeable constant-diameter pipe as the working section (although with various aspect ratios), Vakili, Tennent & Panchapakesan (1996)

observed regime III in an apparatus with tangential fluid injection along the length of the pipe. This diversity of apparatus and the wide parameter range makes comparison between studies difficult; however it is generally agreed that regime III is a product of exceptionally high swirl.

No such agreement exists as to the underlying physical mechanisms involved in regime III flow, possibly because certain aspects are emphasized differently in the various experimental arrangements. Some explanations are posed in terms of axial pressure gradients arising from axial gradients in the azimuthal velocity distribution. These are linked by a balance between centrifugal body forces and the radial pressure gradient. Thus, if there is significant decay of the azimuthal velocity, an adverse pressure gradient is set up near the axis, eventually leading to regime II. More delicate arguments are necessary to explain the onset of regime III. For example, Guo & Dhir (1990) proposed that the large variations of the azimuthal velocity they measured in the vicinity of the swirl generation device were responsible while Nissan & Bresan (1961), whose pipe was relatively long, suggested it was the decay of swirl combined with the squeezing effect due to the development of wall boundary layers. On the other hand, Vakili *et al.* (1996) discuss the possibility that their flow is related to the multi-cellular similarity solutions of Donaldson & Sullivan (1960). Their apparatus approximates the boundary conditions of these solutions (i.e. a rotating porous cylinder) much better than the non-porous pipes used in the other studies. Finally, Binnie (1957) found that unless endwalls were placed in the pipe, it was not possible to achieve regime III. He therefore suggested that the flow reversal in this regime was due to radial flow induced in the endwall boundary layer. As before, this assumes there is a balance between the radial pressure gradient and the centrifugal body force in the external flow. In the boundary layer, the fluid is retarded and the centrifugal body force reduces. A radial flow is established by the action of the external radial pressure gradient. It was suggested that some of this radial flow was somehow forced to move upstream.

The idea that downstream boundary conditions such as an end-plate might be important is supported to some extent by Nuttal's (1953) original experiment where the throttling device used at the outlet affected the swirl intensity at which transition from one regime to the next occurred. Downstream boundary conditions can have a strong upstream influence when the flow is subcritical. Swirling flows are classified as subcritical when infinitesimal axisymmetric waves propagate upstream and supercritical when such waves are swept downstream. Increasing the swirl relative to the axial flow usually drives the flow state from supercritical to subcritical. Analysis of experimental data by Leibovich (1984) suggests that the mean velocity profiles in the wake of vortex breakdown (see below) are subcritical. This follows Benjamin's (1962) original proposal that vortex breakdown is a transition from a supercritical flow state to a conjugate subcritical flow state. Escudier & Keller (1985) investigated the effect of a downstream contraction in a model of a swirl-stabilized combustion chamber consisting of a guide vane mechanism to generate the swirl and a constant-diameter pipe. When the guide vane angle was 62°, axial flow reversal was limited to a vortex breakdown event located close to the pipe inlet. In this case, viscous effects were sufficiently strong that the flow became supercritical upstream of the pipe exit and the addition of a contraction had little effect on the flow pattern. When the guide vane angle was increased to 70°, axial flow reversal was observed on the axis along the entire length of the pipe (regime II). In this case, the flow remained subcritical through to the pipe exit and addition of a contraction caused a transition to unidirectional axial flow and a change in the shape of the breakdown bubble. For a

strong contraction, the flow exhibited an annular axial velocity deficit. It is tempting to interpret this as an early stage of transition to regime III.

Previous studies of regime III flow do not make reference to vortex breakdown, possibly because they predate much of the work on this subject. Vortex breakdown refers to the sudden change in flow structure, usually characterized by strong axial flow deceleration, that can occur in sufficiently swirled flows. Leibovich (1978) distinguishes vortex breakdown from the almost columnar flow regimes described above. The vortex breakdown literature is now extensive and a number of review articles are available (Leibovich 1978, 1984; Escudier 1988; Delery 1994; Althaus, Brücker & Weimer 1995). Note that these omit the comprehensive theoretical study of axisymmetric vortex breakdown contained in a series of articles by Wang & Rusak and their coworkers and summarized in Wang & Rusak (1997*b*). The work to date has greatly clarified the structure and dynamics of vortex breakdown itself, but relatively little attention has been given to the unsteady, three-dimensional flows following vortex breakdown. The experimental works of Harvey (1962) and Escudier & Keller (1985) show that regime II may occur following vortex breakdown, but do not explore a possible transition to regime III. It is possible that the earlier accounts of regime II were associated with vortex breakdown. On the other hand, Leibovich (1978) reports that regime II flow was not observed in the experiments of Faler & Leibovich (1977) and Sarpkaya (1971).

Binnie's (1957) results indicate that, for certain pipe Reynolds numbers, a direct transition from regime I to regime III is possible. This result is consistent with our initial experiments using the tangential jet apparatus (Mattner *et al.* 1996; Mattner 2000). Neither vortex breakdown nor regime II flow were observed but the vortex core deformed into a large-amplitude helical structure as the flow transitioned from regime III to regime I (with decreasing swirl). This transition was relatively abrupt and no incipient stage was evident in the measured velocity profiles. At high swirl, the downstream boundary conditions were found to have a strong effect on the peak axial and azimuthal profiles. A weakness of the jet-driven apparatus was that flow control devices could not be used. The flow consequently suffered from high turbulence intensity and asymmetry, even at zero swirl. This complicated study of the transition process. Furthermore, it was not possible to establish laminar free-vortex velocity profiles of the type usually found in guide vane swirling flow apparatus (e.g. Faler & Leibovich 1977, 1978; Garg & Leibovich 1979; Uchida, Nakamura & Oshawa 1985; Uchida *et al.* 1987). At high swirl, there was limited similarity to the velocity profiles measured by Escudier, Bornstein & Maxworthy (1982) in their slit-jet-driven apparatus (in particular, strong axial jets and increasing circulation outside the core), but their profiles show no evidence of annular axial flow reversal. As a result, it was not possible to establish any explicit connection with the type of flows usually encountered in the vortex breakdown literature.

This study clarifies the transition process leading to regime III using a modified guide vane apparatus. The apparatus and our experimental technique are described in § 2, along with their limitations. In § 3, certain parameters are defined and their limitations discussed. Data processing is also described. The flow at low swirl intensity is described in § 4. The vortex properties are typical of those encountered in guide vane apparatus prior to vortex breakdown. It is shown that the flow behaves like a quasi-cylindrical vortex. The properties of this type of vortical flow have been elucidated by Hall (1967), Beran & Culick (1992) and Wang & Rusak (1997*a*). This common reference flow shows that the apparatus produces a flow which is not unique, unlike the jet-driven flow.

At a slightly higher swirl intensity, an abrupt, localized change in flow structure occurred. These flows are described § 5. It is shown that the flow behaviour is consistent with the unsteady spiral form of vortex breakdown. This was not observed in the jet-driven flow. Previous quantitative experimental studies of spiral vortex breakdown include those by Garg & Leibovich (1979), Uchida *et al.* (1987), Brücker (1993) and Brücker & Althaus (1995). Of these, only Garg & Leibovich (1979) present data from the vortex breakdown wake and this was for a diverging pipe geometry. Rigorous theoretical understanding of the three-dimensional unsteady vortex breakdown wake is extemely limited. Not only is a more thorough study of this topic beyond the scope of the current paper, but the time-averaged measurement techniques used here suffer serious limitations in this type of flow (see § 2).

Measurements of the unsteady flow obtained after vortex breakdown had moved well upstream are presented in § 6. In § 7, it is shown that, at a particular swirl intensity, there is a second abrupt transition where the axial velocity profiles develop an annular deficit. Unlike vortex breakdown, where there was a localized transition from jet-like to wake-like axial velocity profiles, this transition occurred simultaneously thoughout the test section. It is also shown that instabilities begin to develop in the outer flow. Measurements of a completely unsteady vortex exhibiting regime III flow at very high swirl are presented in § 8. The results are discussed in § 9, particularly with regard to the flow state and the work of Escudier & Keller (1985).

2. Experimental apparatus and techniques

In order to address the problems experienced by Mattner *et al.* (1996), the jet-driven apparatus was modified by installation of a guide vane system similar to those used by Sarpkaya (1971) and Faler & Leibovich (1978). This allowed a series of screens and honeycomb to be installed upstream of the guide vanes, thus reducing both the free-stream turbulence intensity and asymmetry (see below) from over 20% to approximately 2% of the bulk axial velocity at zero swirl. The apparatus is shown in figure 1. Water was pumped from a reservoir to the top of the centrepiece via an inlet manifold designed to provide a uniform azimuthal distribution of mass flow. Coarse air-conditioning filter material damped surface waves generated by the turbulent inlet flow. Excess flow passed over an overflow weir and returned to the reservoir, thus fixing the height of the free surface. The remaining flow then turned radially inward to enter the contraction beneath the centrepiece. Two of the screens were arranged to assist this turn while a third was situated immediately following the honeycomb. The honeycomb was formed into an arc to ensure a radial flow incident on the guide vanes. Sixteen guide vanes were arranged uniformly about the circumference of the contraction. The swirl intensity was controlled by the guide vane angle β, defined as the angle between the blade chord and a radial line passing through the pivot (figure 1*b*). Each vane was rigidly fixed to a shaft which was driven by a sprocket and chain mechanism allowing simultaneous adjustment of all guide vane angles. The uncertainty in angular position of the guide vanes was approximately $\pm 0.5^\circ$. The working section was a clear acrylic pipe with uniform radius $R = 86$ mm. Fluid was finally exhausted to the atmosphere through an orifice of diameter 14.25 mm, collected in a bucket, and returned to the reservoir.

The volume flow rate was measured using a bucket and stop watch. Sufficient samples were taken to reduce the precision error to $\pm 1\%$.

Laser Doppler velocimetry was used to obtain mean azimuthal and axial velocity data at nine equidistant stations along the working section of the pipe. The pipe

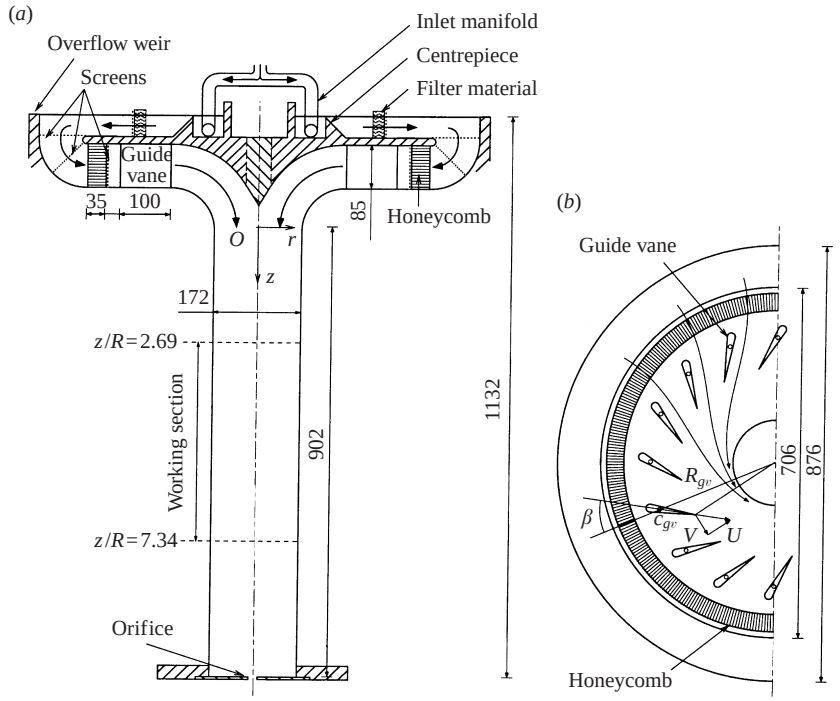

FIGURE 1. Schematic diagram of swirling flow apparatus: (*a*) elevation, (*b*) plan. R is the radius of the pipe and z the axial component of a cylindrical coordinate system whose origin O lies at the start of the straight pipe. β is the guide vane angle. R_{gv} and c_{gv} are geometric parameters equal to 252 mm and 73 mm respectively. U and V are the radial and azimuthal velocity components at the trailing edge of the guide vane respectively. All dimensions in mm. Approximately to scale.

was encased in a square-sectioned enclosure which was filled with water to minimize optical distortion. A TSI 9100-7 two-component optical system was used. This system operates in the dual beam mode with backscatter light detection. The light source was a Spectra Physics model 164 argon ion laser with nominal beam diameter 1.25 mm. Bragg cells were incorporated on each channel to introduce a permanent 40 MHz frequency shift in the Doppler signal. This could be downmixed to produce effective shifts from zero to 10 MHz. Beam spacing prior to entering the transmitting optics was 22 mm. The output optics consisted of a 3.75× beam expander and transmitting lens of focal length 762 mm. The resulting probe volume was approximately 0.1 mm in diameter and 2.5 mm in length.

The green beams (wavelength $\lambda = 0.5145\,\mu$m) were nominally aligned in the vertical plane, parallel to the axis of symmetry of the pipe, and thus measured axial velocity. The blue beams ($\lambda = 0.4880\,\mu$m) were nominally aligned in the horizontal plane and measured azimuthal velocity. The major axis of the probe volume was aligned in the radial direction. The laser and optical system were mounted on a milling machine bed which allowed radial and axial traversing in a meridional plane across the entire diameter of the pipe. Travel limitations restricted measurements to the region $2.69 \leqslant z/R \leqslant 7.34$ shown in figure 1(*a*). The precision of the probe volume position was ± 0.033 mm in the radial direction and ± 0.5 mm in the axial direction. Beam reflections were used to align the vertical axis of the traverse with the axis of symmetry of the pipe to less than $\pm 0.4^\circ$. Similarly, the centre of the pipe measured perpendicular to the optical axis was established to an accuracy of ± 0.6 mm. The

pipe centre measured parallel to the optical axis was established by first locating the wall of the square enclosure from the peak photomultiplier output to an accuracy of ± 0.5 mm, then computing the displacement to the centre of the pipe, taking into account the optical effects of the enclosure, pipe wall and water.

The optical alignment was checked by measuring the velocity at the circumference of a rotating disk. At the centre of the probe volume, the measured calibration constant (fringe spacing) was within $\pm 1\%$ of that calculated from the optical configuration. A variation of $\pm 2\%$ was found over the length of the probe volume; however since this variation was virtually linear its effect on the mean velocity is small. Corrections were devised to account for small angular misalignments of the beam planes parallel and perpendicular to the pipe axis. The effective frequency shift was chosen as a compromise between minimizing the effects of fringe or incomplete signal bias which occurs when the shift is too small and noise and resolution problems when the shift is too large (Patrick 1985). To achieve this, charts were constructed showing the minimum shift necessary to ensure less than 10% directional variation in the probability of detecting a particle. The flow was seeded with silicon carbide particles of mean diameter 1.5 μm and density 3200 kg m^{-3} at a concentration of approximately one particle per probe volume. Using a simple Stokes drag analysis (Drain 1980), these particles have a settling velocity of 3×10^{-6} m s^{-1} and response time of order 4 μs in water. TSI IFA550 counter type processors were used to analyse the Doppler signal. At lower data rates, a sample and hold processor was emulated by storing the digital output and computing the statistics using the burst inter-arrival time as a weighting factor. At higher data rates, the required storage became excessive and controlled processing (even sampling time) techniques combined with arithmetic averages were used instead. For these methods, velocity bias is negligible when $\dot{N}_2 T_u > 5$ (Winter, Graham & Bremhorst 1991*a*) and $\dot{N}_2 T_s > 5$ (Winter, Graham & Bremhorst 1991*b*), where $\dot{N}_2$ is the validated data rate, T_u the integral time scale and T_s the sampling interval used in controlled processing. Rough estimates of T_u obtained from auto-correlations confirmed that the time scales were relatively slow and that the first condition was satisfied by an order of magnitude. The second condition was satisfied by appropriate selection of T_s. Full details of the measurement techniques are reported by Mattner (2000).

The slow time scales created a much less favourable situation for obtaining accurately converged results. Sampling was continued until at least 5000 samples were collected or a minimum sample time T was achieved. T varied from 60 s in steady laminar flow up to 240 s in unsteady flow. Convergence histories indicate random relative errors of less than $\pm 2.5\%$ of the peak velocity for most of the data. One exception occurred close to the centre of the vortex for $\beta \geqslant 46^\circ$ where slow meandering of the core caused variation in the mean velocity of up to $\pm 5\%$. Another occurred in the vicinity of vortex breakdown where fluctuations in the mean of up $\pm 10\%$ were observed on a time scale of order T. This was caused by the slow, quasi-periodic meandering of the disturbance along the pipe axis combined with large axial gradients of velocity. This is a common problem with the measurement of vortex breakdown flows (Faler & Leibovich 1978) and seriously limits the ability of standard time-averaged measurements to discern the detailed flow structure.

The flow was very sensitive and stopping the apparatus between stations led to small discontinuities in the data. For this reason, the apparatus was operated continuously and measurements acquired over several days. Another significant source of variation was due to fluctuations in the laboratory temperature. Although the water temperature T_{H_2O} varied less than $\pm 0.1\,^\circ$C, it was necessary to operate at an elevated

temperature ($T_{H_2O} \sim 28\,^{\circ}\mathrm{C}$) so that a simple heat exchanger used to control T_{H_2O} could function effectively. It was found that the free-stream axial velocity increased by about 1% per degree Celsius increase in laboratory temperature. Variations of approximately 2–3 °C were often encountered over the several days required to complete a set of measurements, due mainly to changing weather patterns and inadequate air conditioning. This behaviour is consistent with the development of thermal boundary layers on the pipe walls.

The vortex centreline was established using the radial position of zero azimuthal velocity and the lateral displacement of the traverse necessary to place the probe volume on a filament of dye introduced at the apex of the centrepiece. The maximum deviation from the nominal pipe centreline was $|\Delta r| = 2\,\mathrm{mm}$ or $|\Delta r/R| = 0.023$, a figure greater than the uncertainty in locating the pipe centre. Consequently, the flow is not perfectly axisymmetric; however if the origin is shifted to the vortex centreline, the free-stream asymmetry (as determined by the variation between the velocities measured at the azimuthal locations $\theta = 0$ and π) was less than 2% of the bulk axial velocity at $\beta = 19^{\circ}$. Lateral misalignment of the measurement plane with the vortex centreline tends to reduce measured peak velocities (Escudier *et al.* 1982). For the maximum observed deflection, this error varies from 2% of ΔW for $\beta \leqslant 26^{\circ}$ (where $\Delta W = W_{max} - W_{min}$ and W is the mean axial velocity) up to 5% of ΔW at $\beta = 69^{\circ}$ where the vortex core is particularly narrow (for full details, see Mattner 2000).

Wall approach limitations prevented mean flow measurements from being extended into the pipe wall boundary layers with the same level of confidence as the remaining data. By relaxing some constraints normally imposed on the measurements, it was possible to obtain limited data at $\beta = 0^{\circ}$ and 19°. Integration of the axial velocity profiles yielded volume flow rates which underestimated the true values by 4.5% and 1.5% respectively. These discrepancies are thought to be due to azimuthal non-uniformities in the boundary layer thickness caused by the upstream effects of the guide vanes.

Accurate turbulence measurements were prevented by noise introduced as a result of fringe space variation along the probe volume and velocity gradient broadening which together contributed to at least half the measured variance for $\beta \leqslant 19^{\circ}$. The second problem was exacerbated by the rather long probe volume and its alignment in the direction of large radial gradients of velocity.

3. Definitions and flow parameters

3.1. *Coordinate system*

Data are presented in terms of a cylindrical coordinate system with radial, azimuthal and axial components (r, θ, z) respectively. The origin O is located at the beginning of the pipe (figure 1*a*). The corresponding velocity components are $(u = U + u', v = V + v', w = W + w')$ where capital letters denote the mean and primes the fluctuating part.

3.2. *Flow parameters*

The volume flow rate Q at each swirl intensity is shown in table 1. The mean volume flow rate was $0.525 \times 10^{-3}\,\mathrm{m^3\,s^{-1}}$ and individual measurements differed from this by less than $\pm 1.2\%$ over the entire range of β. This variation is not much larger than the measurement uncertainty and any correlation between Q and β is extremely weak.

β (deg.)	$Q\,(\mathrm{m^3\,s^{-1}})$	$W_b\,(\mathrm{m\,s^{-1}})$	$\Gamma_0\,(\mathrm{m^2\,s^{-1}})$	Ω	Re
0	0.521×10^{-3}	0.0224	0.0	0.0	4859
19	0.521×10^{-3}	0.0224	0.00303	0.79	4859
23	0.527×10^{-3}	0.0226	0.00383	0.98	4915
25	0.525×10^{-3}	0.0226	0.00422	1.09	4896
26	0.522×10^{-3}	0.0224	0.00440	1.14	4868
29	0.525×10^{-3}	0.0226	0.00510	1.31	4896
39	0.529×10^{-3}	0.0227	0.00840	2.05	4934
44	0.526×10^{-3}	0.0226	0.00997	2.56	4906
45	0.527×10^{-3}	0.0226	0.0105	2.68	4915
46	0.527×10^{-3}	0.0226	0.0110	2.81	4915
69	0.531×10^{-3}	0.0228	0.0846	21.5	4953

TABLE 1. Flow parameters.

The bulk axial velocity W_b is defined by

$$W_b = \frac{Q}{\pi R^2} \tag{3.1}$$

and the pipe Reynolds number Re by

$$Re = \frac{2W_b R}{\nu} \tag{3.2}$$

where ν is the kinematic viscosity. The variation in Re due to temperature (and hence viscosity) fluctuations of $\pm 0.1\,^{\circ}\mathrm{C}$ was about $\pm 0.2\%$.

In order to be consistent with previous studies of vortical flow employing guide vane mechanisms (e.g. Sarpkaya 1971; Faler & Leibovich 1978), the swirl intensity Ω is defined by

$$\Omega = \frac{\Gamma_0}{2RW_b} \tag{3.3}$$

where Γ_0 is the circulation at the trailing edge of the guide vanes. This is estimated by assuming that the flow at the trailing edge is uniform in both the azimuthal and axial directions and parallel to the guide vane chord. The circulation is then $\Gamma_0 = 2\pi R_{te} V$ and the flow rate $Q = 2\pi R_{te} H U$ where H is the guide vane span ($H = 85\,\mathrm{mm}$, see figure 1a), U and V the radial and azimuthal velocity components at the trailing edge respectively and R_{te} the distance from the trailing edge to the axis of symmetry. Using the geometry shown in figure 1(b) to find the relationship between U and V and to determine R_{te}, it can be shown that

$$\Gamma_0 = \frac{Q}{H} \frac{\sin\beta}{\cos\beta - c_{gv}/R_{gv}} \tag{3.4}$$

where c_{gv} is the distance from the pivot of the guide vane to its trailing edge and R_{gv} the distance from the pivot to the axis of symmetry.

The validity of equation (3.4) does not appear to have been questioned in the literature. One problem is that it suggests $\Gamma_0 \to \infty$ as $\cos\beta \to c_{gv}/R_{gv}$ ($\beta \to 73.2^{\circ}$ in the present apparatus). This indicates that for sufficiently large β the assumptions on which equation (3.4) is based must fail, possibly by flow separation for example. Another problem is that in some studies the circulation further downstream actually exceeds that predicted by equation (3.4) by a significant margin. For example, the

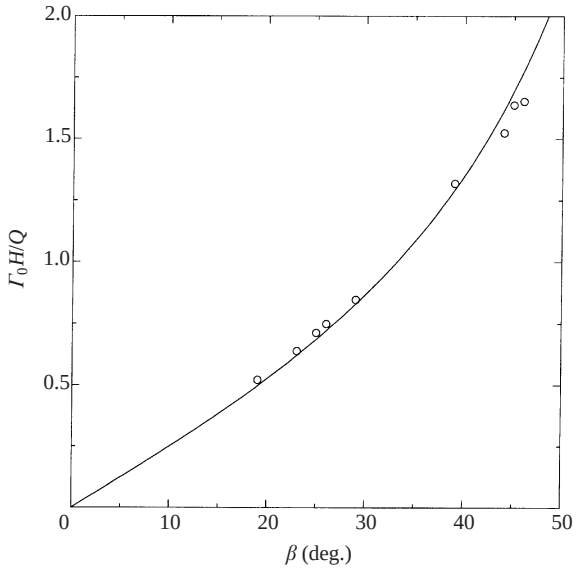

FIGURE 2. Comparison of circulation estimated from equation (3.4) (solid line) with experimental data.

experimental data of Faler & Leibovich (1978) indicates an overshoot of 38% while there is an overshoot of 26% in the numerical simulation of a complete guide vane apparatus by Snyder & Spall (2000). Figure 2 compares the circulation measured outside the vortex core and wall boundary layers with the estimate from equation (3.4). For $\beta \leqslant 39^\circ$ there is an overshoot of about 5%. This is not much greater than the uncertainty associated with the scatter of $\pm 2\%$ due to minor asymmetries and the variation evident in the plateau region of up to 4% (see § 4). A horizontal shift of 0.6° provides a least-squares fit of the data up to $\beta = 39^\circ$ with equation (3.4). This shift is comparable to the uncertainty in β. Thus, considering the experimental uncertainty, equation (3.4) provides a satisfactory estimate of Γ_0 for $\beta \leqslant 39^\circ$. Alternatively, the overshoot can be explained by the displacement effect of the boundary layers on the contraction and centrepiece walls and the guide vanes themselves. This would tend to accelerate the radial flow and thus increase the circulation. If we neglect the guide vane boundary layer, then equation (3.4) may be modified by replacing H with $H - 2\delta^*$ where δ^* is the displacement thickness of the boundary layers on the contraction and centrepiece walls. A 5% increase in the circulation is consistent with a displacement thickness of about 2 mm, which is the correct order of magnitude. For $\beta \geqslant 44^\circ$ the difference between the data and equation (3.4) cannot be explained by experimental error or a consideration of wall boundary layers. Note that the data at $\beta = 69^\circ$ is omitted for clarity, but equation (3.4) overestimates the circulation by at least a factor of three. In this case the comparison is complicated by the absence of any plateau in the circulation profile as a result of outer flow unsteadiness.

3.3. *Data presentation and analysis*

The mean azimuthal and axial velocity fields are presented as quasi-vector plots (figure 3, for example) to help give a quick overall impression of the flow. The arrows are drawn at every second data point and indicate displacement of the velocity from zero. The actual profiles (solid line) are constructed as piecewise linear curves connecting all data points. Only for the axial velocity component do the arrows

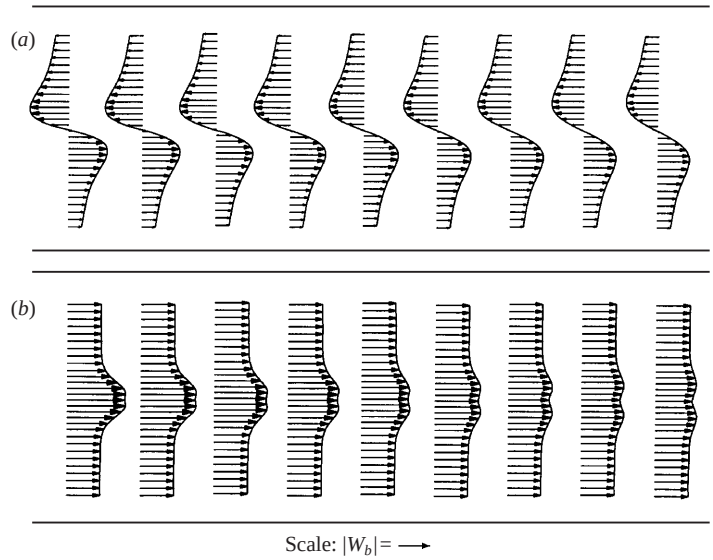

FIGURE 3. (*a*) Azimuthal and (*b*) axial velocity profiles for $\beta = 23°$, $\Omega = 0.98$, $Re = 4915$.

show the mean flow direction, with positive axial flow down the pipe. Note that each diagram has been rotated by 90° so that the positive z-direction is from left to right. The scale of the arrows is shown at the bottom of each diagram in terms of W_b. The horizontal line to either side of the profiles indicates the position of the pipe walls in the measurement plane. The aspect ratio of these diagrams is correct.

Subsequent analysis is facilitated by generating representative axisymmetric velocity profiles at each station. This was done by shifting the origin to the centre of the vortex (so that $V = 0$ at $r = 0$) and calculating the azimuthal average

$$\langle X \rangle(r_i) = \frac{X_{\theta=0}(r_i) + X_{\theta=\pi}(r_i)}{2} \tag{3.5}$$

where X is the variable being averaged and r_i the radius of the ith data point. Linear interpolation was used between data points. Sensitivity to the assumption of axisymmetry was assessed by re-computing with the data at $\theta = 0$ and π separately. Note that calculation of the circulation Γ around the circular path C of radius r using

$$\Gamma(r) = \oint_C \boldsymbol{U} \cdot \mathrm{d}\boldsymbol{s} = \int_0^{2\pi} rV \,\mathrm{d}\theta = 2\pi rV \tag{3.6}$$

assumes the flow to be axisymmetric. The same assumption applies to the stream function ψ defined by

$$U = -\frac{1}{r}\frac{\partial \psi}{\partial z} \quad \text{and} \quad W = \frac{1}{r}\frac{\partial \psi}{\partial r} \tag{3.7}$$

and calculated from

$$\psi(r) = \int_0^r \hat{r} W(\hat{r}) \,\mathrm{d}\hat{r} \tag{3.8}$$

with $\psi(0) = 0$ and $\psi_0 = \psi(R) = Q/2\pi$.

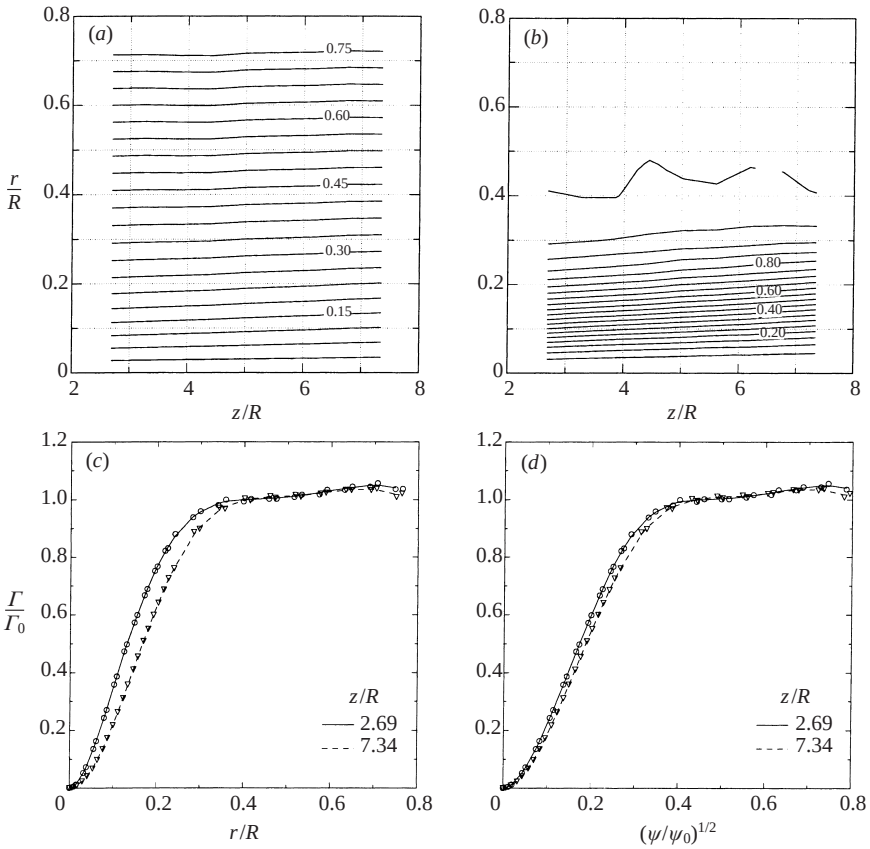

FIGURE 4. Streamwise variation of ψ and Γ for $\beta = 23°$. (a, b) Isolines of $\langle \psi/\psi_0 \rangle$ and $\langle \Gamma/\Gamma_0 \rangle$ respectively. (c, d) The solid and dashed lines refer to azimuthally averaged data while the discrete symbols refer to unaveraged data.

4. Laminar, steady flow

For $\beta \leqslant 23°$, dye introduced at the apex of the centrepiece flowed as a steady and undisturbed filament along the pipe centreline. The velocity profiles at $\beta = 23°$ are shown in figure 3. The qualitative trends at $\beta = 19°$ were similar. At this swirl intensity, the azimuthal velocity profiles are qualitatively similar to a Burgers vortex while the upstream axial velocity profile exhibits a central peak or jet. Both these characteristics are typical of vortices produced by guide vane apparatus upstream of vortex breakdown (cf. Faler & Leibovich 1977, 1978; Garg & Leibovich 1979; Uchida *et al.* 1985, 1987). Faler & Leibovich (1977) attribute the former to the radial inflow of an essentially irrotational flow with circulation Γ_0. To examine this more closely, figure 4(c) shows typical circulation profiles for the same flow case, $\beta = 23°$. As the axial vorticity ζ is related to the radial variation of Γ by $\zeta = (1/r)(\partial\Gamma/\partial r)$, this figure confirms that axial vorticity was concentrated in the core as in a Burgers vortex. On the other hand, a 4% increase in Γ between the core and the wall boundary layers (the plateau between $0.4 \leqslant r/R \leqslant 0.7$) shows that the outer flow was not perfectly irrotational. The source of this weak background axial vorticity is not known. Note that circulation plots are particularly sensitive to variations in the outer flow. The relatively small scatter of up to $\pm 2\%$ in the unaveraged data suggests that the flow is nearly axisymmetric.

The jet-like axial velocity profile is often explained as the result of the conservation of total head and the pressure minimum at the centre of the vortex (e.g. Escudier 1988). The jet is associated with positive azimuthal vorticity η, since for quasi-cylindrical flow $\eta \approx -\partial w/\partial r$, yet the azimuthal vorticity component generated at the centrepiece walls is expected to be negative. To explain this, consider steady incompressible axisymmetric inviscid flow. Brown & Lopez (1990) show that for a stream surface of radius $r = \sigma$,

$$\frac{\eta}{\eta_0} = \frac{\sigma_0}{\sigma}\left(\frac{\alpha_0}{\beta_0}\right) - \frac{\sigma}{\sigma_0}\left(\frac{\alpha_0}{\beta_0} - 1\right), \tag{4.1}$$

where $\alpha_0 = v_0/w_0$ and $\beta_0 = \eta_0/\zeta_0$ are the upstream values of the tangents of the helix angles of velocity and vorticity respectively and the subscript 0 denotes values at an upstream station. If $\eta_0 < 0$ then $\alpha_0/\beta_0 < 0$ (assuming all other terms are positive) and for sufficiently small values of σ/σ_0 (strongly converging flow), $\eta/\eta_0 < 0$, i.e. $\eta > 0$. Thus, it is possible to explain the axial velocity jet in terms of the distortion of vortex filaments generated at the centrepiece wall by the strongly converging flow within the contraction. For vorticity generated near the apex of the centrepiece, the convergence σ/σ_0 would be relatively small and η may remain negative. It is therefore not surprising to find a small axial velocity deficit superimposed on the jet very close to the centre of the vortex (figure 3). This feature is also apparent in some of the profiles of Faler & Leibovich (1978) upstream of vortex breakdown.

For $\beta \leqslant 23^\circ$, the flow developed slowly with streamwise distance. The most obvious variation evident from figure 3 is the gradual decay of the peak azimuthal and axial velocities. This is associated with a gradual divergence of the stream surfaces and vortex tubes, particularly near the centre of the vortex. This divergence is relatively slight and is shown most clearly by plotting isolines of ψ and Γ as in figures 4(a) and 4(b) respectively. The radial re-distribution of Γ is due to a combination of viscous diffusion and convection of vorticity by the diverging flow. Figure 4(d) shows Γ/Γ_0 plotted versus $(\psi/\psi_0)^{1/2}$ for the first and last stations. Note that the function $(\psi/\psi_0)^{1/2}$ is equal to r/R for uniform axial flow and exposes details near $r = 0$ more clearly than simply plotting versus ψ/ψ_0. If the flow were steady axisymmetric and inviscid, $\Gamma = \Gamma(\psi)$ and the data would collapse onto a single curve. In the absence of significant unsteadiness or asymmetry, the decrease of $\Gamma(\psi)$ with streamwise distance is indicative of viscous diffusion. As there is no significant externally applied adverse pressure gradient or streamline divergence, it might be thought that this process would be dominant. However, comparison of figure 4(d) with figure 4(c) suggests that the streamwise variation of $\Gamma(\psi)$ is weaker than the streamwise variation of $\Gamma(r)$ and hence that convective transport is also significant. The importance of both convective and diffusive effects in a flow where radial variations dominate axial variations is consistent with the quasi-cylindrical (boundary layer) approximation of Hall (1966).

It is possible to obtain convincing agreement between solutions of the quasi-cylindrical equations and the data. The quasi-cylindrical equations are parabolic and can be integrated in the streamwise direction, starting from initial azimuthal and axial velocity profiles. It is therefore necessary to obtain an accurate curve fit to data at the upstream station to use as an initial condition. The popular Q-vortex model (Leibovich 1984), given by

$$V = \frac{K_1}{r}[1 - \exp(-\alpha_1 r^2)], \tag{4.2a}$$

$$W = W_0 + W_1 \exp(-\alpha_1 r^2), \tag{4.2b}$$

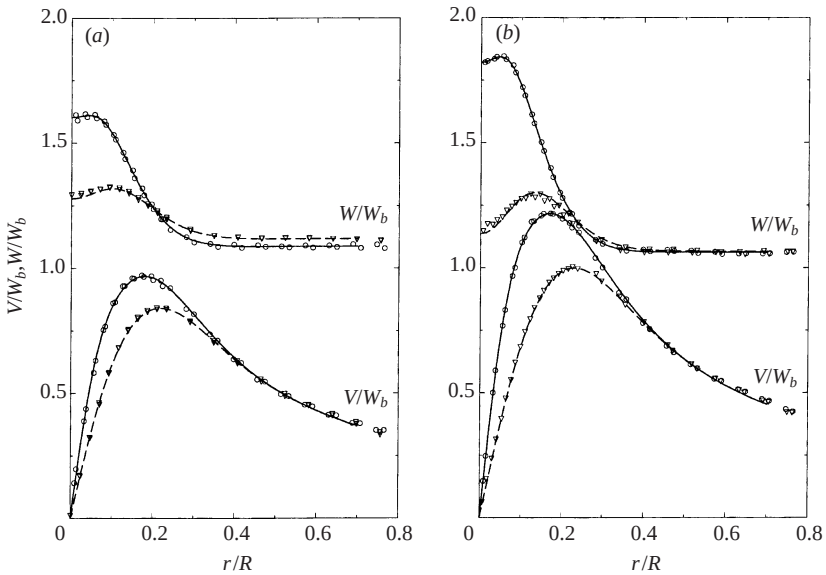

FIGURE 5. Comparison between experimental data and: curve fits using equation (4.3) at $z/R = 2.69$ (solid lines); profiles calculated using the quasi-cylindrical equations at $z/R = 7.34$ (dashed lines) for (*a*) $\beta = 19°$ and (*b*) $\beta = 23°$.

where K_1, α_1, W_0 and W_1 are empirically determined parameters, cannot capture the axial velocity deficit at the centre of the jet or the varying circulation outside the core. A more general model is

$$V = \sum_{i=1}^{M} \frac{K_i}{r}[1 - \exp(-\alpha_i r^2)], \tag{4.3a}$$

$$W = W_0 + \sum_{i=1}^{M} W_i \exp(-\beta_i r^2), \tag{4.3b}$$

where K_i, α_i, W_i and β_i are empirically determined parameters. Devenport *et al.* (1996) obtained close fits to their data by fixing α_i and β_i and using a large number of terms M. The solid lines in figures 5(*a*) and 5(*b*) are least-square fits of equation (4.3) to the data at $z/R = 2.69$ with α_i and β_i variable and only $M = 2$ terms. Note that equation (4.3) can provide a reasonable fit to all the data in this paper with $M \leqslant 3$; however the parameters are sometimes dependent on the initial estimate used in the nonlinear curve fitting process and can vary considerably. Listing all the coefficients would be voluminous, hence they are omitted. The subsequent development of these fitted curves was computed using the finite difference method outlined by Beran & Culick (1992). The outer boundary was fixed at $r/R = 0.7$ and boundary conditions for u estimated from experimental values of ψ and finite difference evaluation of $u = -(1/r)\,\partial\psi/\partial z$ (equation (3.7)). The dashed lines in figures 5(*a*) and 5(*b*) show the calculated profiles at $z/R = 7.34$ using 200 radial nodes and 1000 nodes between axial stations. Despite the crude boundary treatment, it is evident that at these swirl intensities and a Reynolds number of approximately 4900, the flow develops as a quasi-cylindrical vortex. The properties of such vortices have been elucidated by Hall (1967), Beran & Culick (1992) and Wang & Rusak (1997*a*). The latter study indicates that, for sufficiently high core Reynolds numbers, large-amplitude disturbances are induced by viscous effects at a swirl intensity close to critical and the assumptions

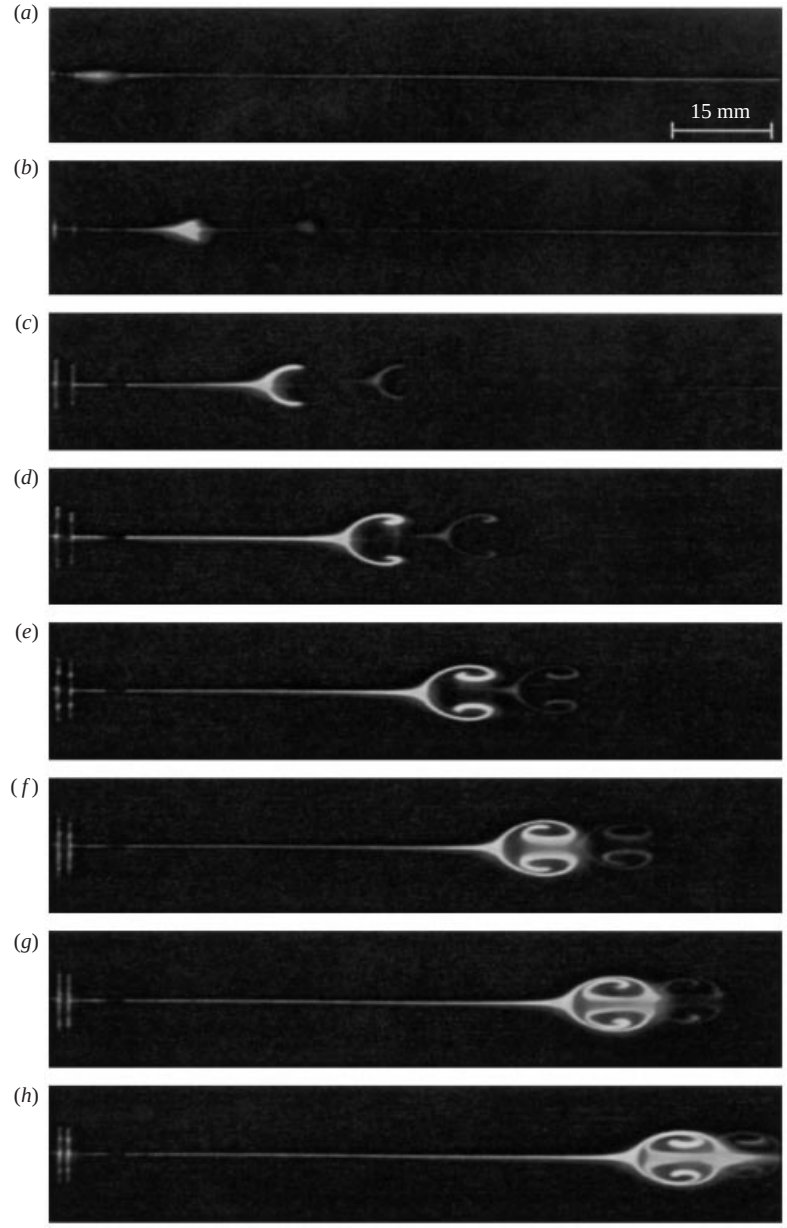

FIGURE 6. Laser cross-section of fluorescent dye showing transient behaviour for $\beta = 26^\circ$, $\Delta\beta = 2.2^\circ$, $Re = 3970$. (*a*) $\Delta t = 0$ s, (*b*) 2 s, (*c*) 4 s, (*d*) 6 s, (*e*) 8 s, (*f*) 10 s, (*g*) 12 s, (*h*) 14 s. Note that Δt is the time measured from the first frame shown.

of the quasi-cylindrical equations are violated. This provides an explanation for the change in behaviour described in the following section and the difficulty of finding numerical solutions to the quasi-cylindrical equations close to critical flow states.

5. Transitional flow I: vortex breakdown

For $\beta \approx 20^\circ$, a sudden increase in β led to the formation of transient structures such as those shown in figures 6 and 7. The precise details of these structures depended

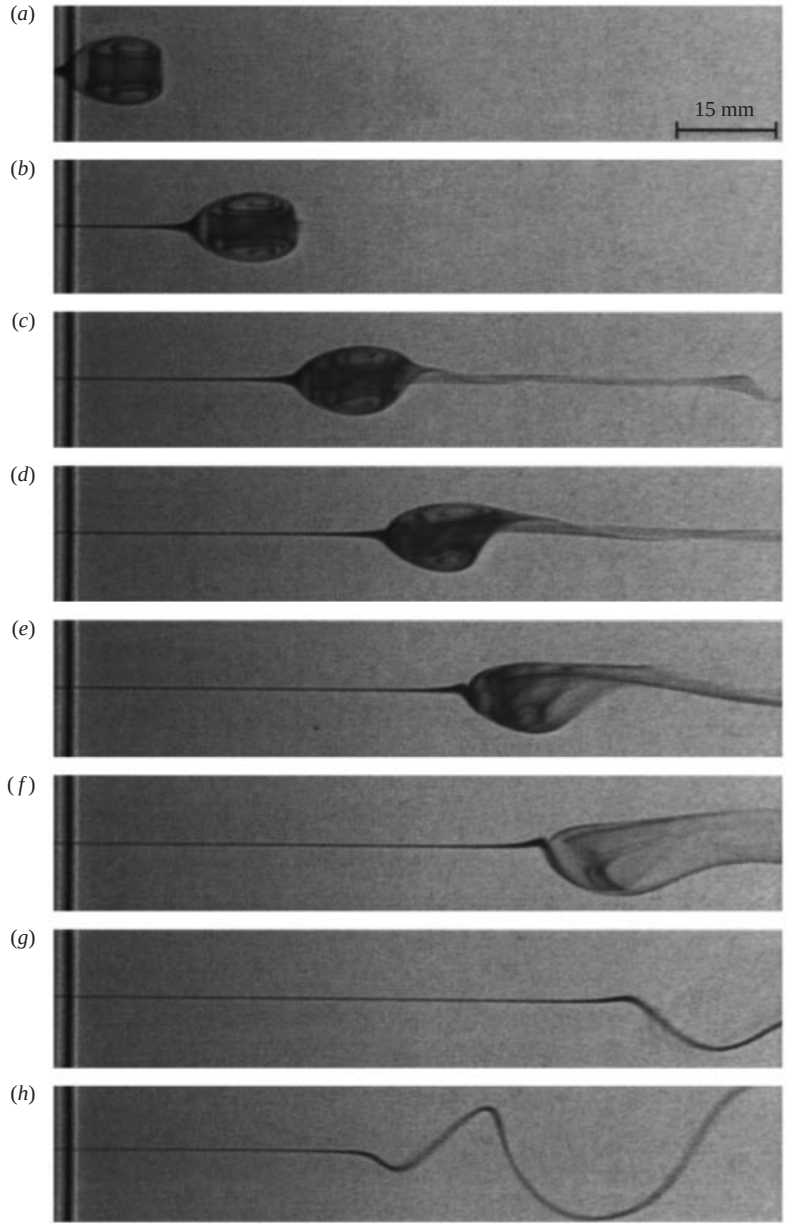

FIGURE 7. Transient behaviour for $\beta = 26°$, $\Delta\beta = 2.8°$, $Re = 4090$. (*a*) $\Delta t = 0$ s, (*b*) 4 s, (*c*) 8 s, (*d*) 12 s, (*e*) 16 s, (*f*) 20 s, (*g*) 24 s, (*h*) $\Delta t \to \infty$, ultimate behaviour for $\beta = 32°$. Note that Δt is the time measured from the first frame.

on the magnitude of β, the increase $\Delta\beta$ and how suddenly the change was applied. Nevertheless, a reasonably consistent qualitative pattern emerges and the figures represent typical behaviour.

The first effect observed after changing β was the momentary non-axisymmetric displacement of the dye filament from its initial position. The amplitude of this displacement was in the order of 2 mm. The disturbance was washed downstream and the filament returned to its initial position. After a further delay, at least one

axisymmetric bulge developed on the filament (figure 6*a*). As this bulge travelled downstream, it increased in amplitude (figure 6*b*) and developed into a ring-like structure (figure 6*c–h*). For sufficiently small β and $\Delta\beta$, this disturbance decayed and was swept out of the apparatus. When β and $\Delta\beta$ were sufficiently large, the ring-like structure grew and the number of internal turns increased (figure 7*a*, *b*) until it developed a periodic, non-axisymmetric wobble (figure 7*c*). The amplitude of this wobble increased (figure 7*c–f*) until the filament of dye became a distinct spiral (figure 7*g*). The spiral rotated in the same sense as the fluid particles but was wound in the opposite sense. The spiral disturbance was swept out of the apparatus or, when β was sufficiently large, eventually meandered very slowly about an equilibrium position within the pipe (figure 7*h*). As β was increased further, the equilibrium position of the spiral disturbance moved upstream, its pitch decreased and the rate of rotation increased.

There are strong similarities between these structures and the initiation and development of vortex breakdown observed in the experiments of Sarpkaya (1971), Faler & Leibovich (1977), Escudier (1988) and Brücker & Althaus (1995). The sequence of events is similar to the scenario proposed by Leibovich (1984) to explain the onset of non-axisymmetric perturbations in vortex breakdown. That scenario related to flow in a diverging pipe at fixed swirl with a disturbance introduced from downstream; here the pipe radius is fixed, the swirl increases and the disturbance appears upstream. Nevertheless, Leibovich describes how weak non-axisymmetric disturbances are first washed downstream, leaving an axisymmetric perturbation which grows in amplitude, eventually becoming unstable to non-axisymmetric perturbations. In a reference frame moving with the disturbance, the axisymmetric structures appear to be related to the steady inviscid axisymmetric nonlinear solitary waves and wavetrains studied theoretically and numerically by Leibovich (1970) and Leibovich & Kribus (1990). Wang & Rusak (1996*b*) have shown that these non-columnar flow states are unstable to a general axisymmetric mode of disturbance. However, under certain conditions, numerical experiments by Rusak, Wang & Whiting (1998*a*) show transient solitary waves developing from perturbed inviscid axisymmetric swirling flows. Depending on the swirl intensity and the magnitude of the initial perturbation, the disturbances are washed out of the domain and the flow returns to its initial columnar state, as in the experiments. Alternatively, the flow develops to a new state, consisting of a steady elongated axisymmetric stagnation zone extending to the outlet of the domain. The dye patterns are not consistent with such a stagnation zone and suggest that the transient structures become unstable to three-dimensional instabilities before such a state can be realized. The stability of the waves calculated by Leibovich & Kribus (1990) was also examined by Kribus & Leibovich (1994) using periodic perturbations which included non-axisymmetric modes. They found that when the amplitude of the waves becomes sufficiently large, stability is initially lost to modes with azimuthal wavenumber ± 1 and that the maximum perturbations are concentrated at the rear of the wave. They describe the motion produced by these modes as 'bending' or 'sloshing'; the latter term is a particularly accurate description of the behaviour at the rear of the bubble in figures 7(*c*) and 7(*d*). The theoretical results suggest that with finer control of β and smaller disturbances, the evolution may be different.

Quantitative experimental studies of vortex breakdown in guide vane apparatus often employ diverging pipes or nozzles to create an adverse pressure gradient. Such devices promote a disproportionate axial velocity deceleration in the core through inviscid pressure or vorticity mechanisms (e.g. Escudier 1988; Brown & Lopez 1990). Many theoretical studies of vortex breakdown focus specifically on vortical

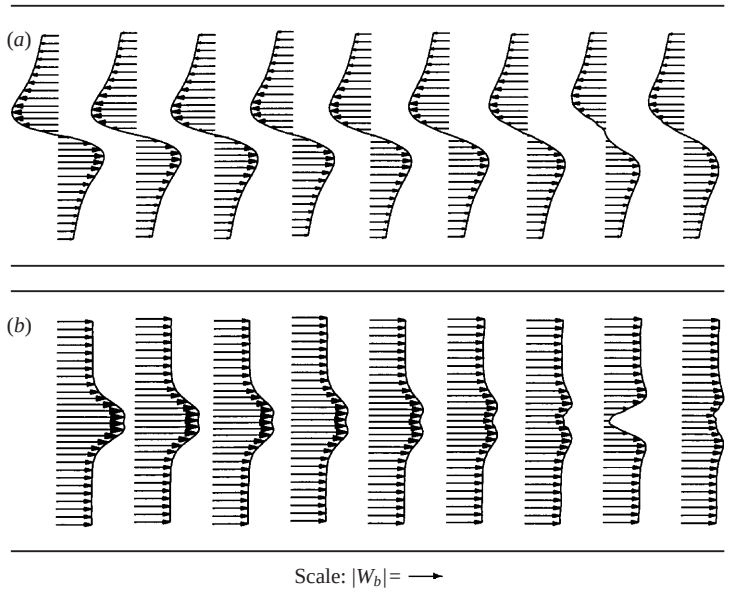

FIGURE 8. (*a*) Azimuthal and (*b*) axial velocity profiles for $\beta = 25°$, $\Omega = 1.09$, $Re = 4896$.

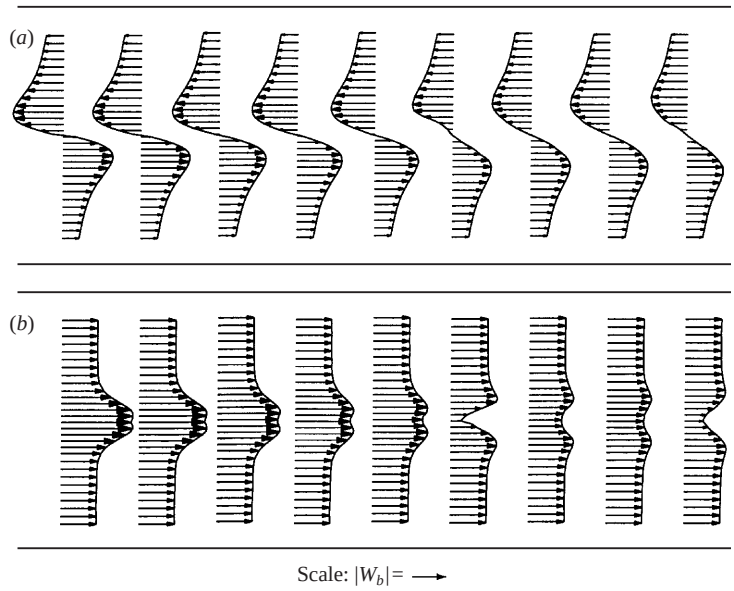

FIGURE 9. (*a*) Azimuthal and (*b*) axial velocity profiles for $\beta = 26°$, $\Omega = 1.14$, $Re = 4868$.

flow through a constant-diameter pipe (e.g. Benjamin 1962; Wang & Rusak 1997*b*). Quantitative experimental studies of this case include the laser Doppler velocimetry measurements of Uchida *et al.* (1985) and Uchida *et al.* (1987) for the axisymmetric bubble and spiral breakdowns respectively. The first of these focuses on the structure of the breakdown bubble itself, while the second only includes data upstream of spiral breakdown. Figures 8, 9 and 10 show the mean flow for $\beta = 25°$, $26°$ and $29°$ respectively. These angles were chosen such that the spiral disturbance occupied the maximum possible range of observable equilibrium positions. It was therefore

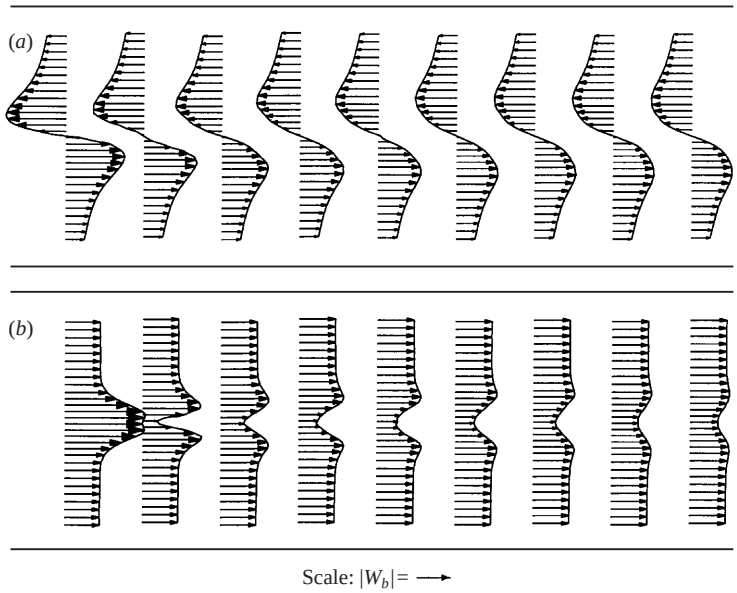

FIGURE 10. (*a*) Azimuthal and (*b*) axial velocity profiles for $\beta = 29°$, $\Omega = 1.31$, $Re = 4896$.

possible to observe the evolution of the vortex far upstream and downstream of the disturbance. Far upstream, the vortex was steady and developed gradually with streamwise distance as before. The beginning of the spiral was associated with a sharp transition from a jet-like to wake-like axial velocity profile (i.e. axial velocity deficit near the axis of symmetry). The outer flow was almost unaffected by this transition.

Solutions to the quasi-cylindrical equations could be progressed some distance downstream of the disturbance; however departures from the experimental data occurred some distance upstream. Thus the quasi-cylindrical assumption failed to be a valid approximation prior to failure of the solution procedure. As Lopez (1994) points out, the quasi-cylindrical equations do not model the inviscid positive feedback mechanism of Brown & Lopez (1990) that is responsible for the rapid flow divergence and deceleration associated with vortex breakdown. The sudden deceleration and change in flow structure is consistent with most descriptions of vortex breakdown. In particular, the wake-like velocity profiles are consistent with those measured by Garg & Leibovich (1979) downstream of spiral vortex breakdown in a diverging pipe geometry. Leibovich (1978, 1984) define vortex breakdown as 'a disturbance characterized by the formation of an internal stagnation point on the vortex axis, followed by reversed flow in a region of limited axial extent'. None of these figures, nor the finer-resolution plots of the centreline axial velocity in figure 12, indicate precise axial flow stagnation or reversal in the mean flow; however the time records confirm transient flow reversal. The core expansion ratio, defined as the ratio of the radial position of maximum azimuthal velocity in the wake flow to that in the approach flow, was in the range 1.2–1.8 (depending on which profiles were chosen). This is in a similar range to those reported by Leibovich (1984) for spiral vortex breakdown in a divergent pipe and less than that normally associated with axisymmetric breakdown.

Figures 11(*a*) and 11(*b*) show isolines of the stream function and circulation for $\beta = 26°$. Note that these are time-averaged quantities downstream of the disturbance where the flow is unsteady. Note also that the axial resolution of the measurements

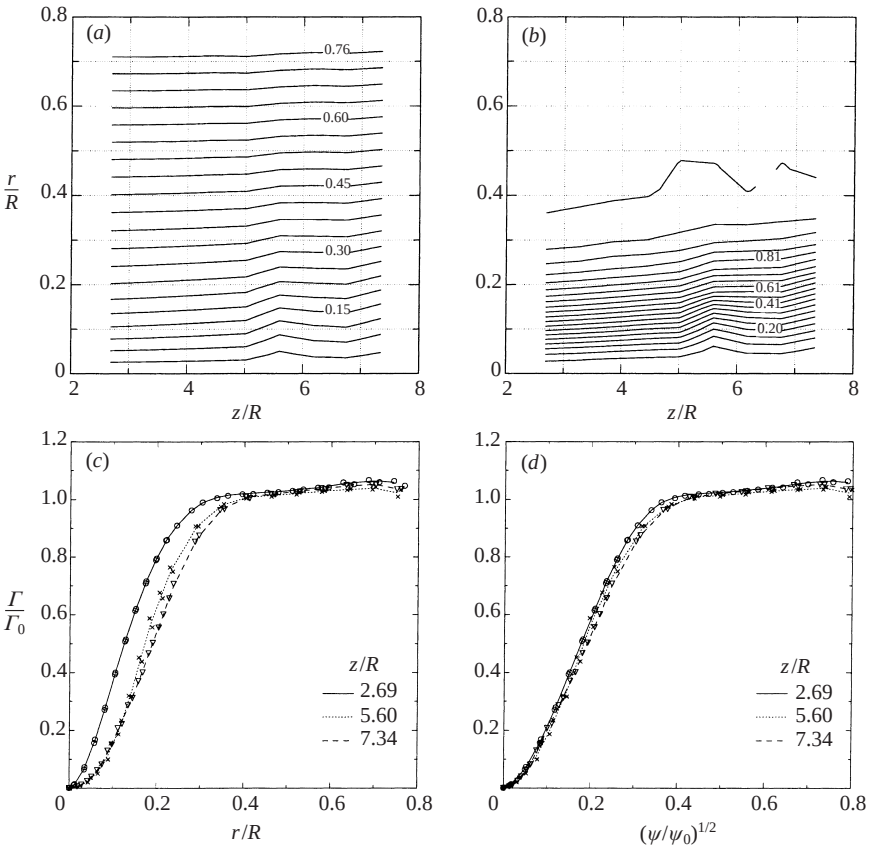

FIGURE 11. Streamwise variation of ψ and Γ for $\beta = 26°$. (a,b) Isolines of $\langle \psi/\psi_0 \rangle$ and $\langle \Gamma/\Gamma_0 \rangle$ respectively. (c,d) The solid, dashed and dotted lines refer to azimuthally averaged data while the discrete symbols refer to unaveraged data.

was coarse and the diagrams do not accurately depict axial gradients close to the disturbance. The figures show that the sudden expansion of the mean stream surfaces correlates well with an expansion of the mean vortex tubes. To see this more clearly, figures 11(c) and 11(d) show Γ/Γ_0 versus r/R and $(\psi/\psi_0)^{1/2}$ for the first and last stations, as well as the first station following the disturbance. There is some streamwise variation of $\Gamma(\psi)$; however it is considerably weaker than that of $\Gamma(r)$. Indeed, a comparison of figures 4(d) and 11(d) suggests that the streamwise variation of $\Gamma(\psi)$ is no greater than that observed in steady flow conditions at $\beta = 23°$. Similar results were found for the other breakdown cases $\beta = 25°$ and 29°. It is not possible to distinguish the effects of viscosity from those of unsteadiness on plots of $\Gamma(\psi)$; however it appears that the additional effect of unsteadiness was relatively small. This is not always the case: unsteadiness in the outer flow at $\beta = 69°$ causes significant streamwise variation of $\Gamma(\psi)$ (figure 22).

The axial velocity profiles (figure 9b), stream function and circulation diagrams (figure 11a,b) for $\beta = 26°$ exhibit a second deceleration and expansion at the last station. To investigate this further, higher-resolution streamwise traverses of the centreline axial velocity were conducted. The results for $\beta = 26°$ and 29° are shown in figure 12. At $\beta = 26°$, there is a single oscillation of wavelength $\lambda/R \sim 1.5$ which correlates well with the data in the previous figures. At $\beta = 29°$, the initial wavelength

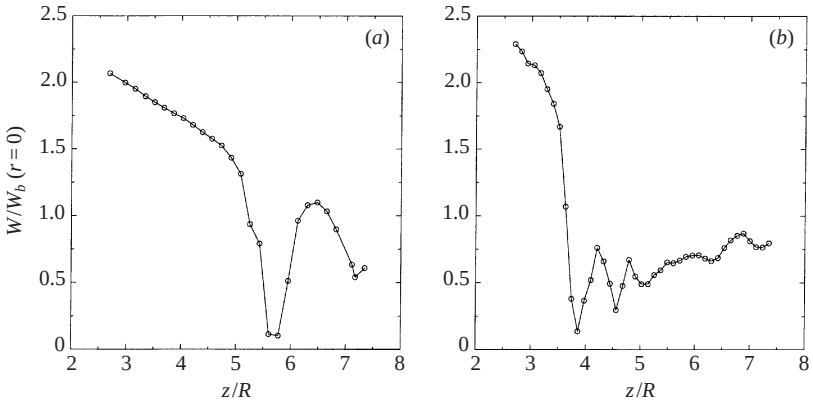

FIGURE 12. Centreline axial velocity for (*a*) $\beta = 26°$ and (*b*) $\beta = 29°$.

$\lambda/R \sim 0.7$ is comparable to the streamwise spacing of the measurement stations $\Delta z/R = 0.58$. Thus the axial resolution of figure 10 was too coarse to resolve the oscillations. The centreline axial velocity is affected only by the axisymmetric mode (Leibovich 1984), hence these figures suggest a stationary wave in that mode. The mean flow downstream of the disturbance is subcritical and therefore capable of supporting small-amplitude finite-wavelength axisymmetric waves. Benjamin (1962, 1967) suggested theoretically the possibility of wavetrains forming in the wake of vortex breakdown, albeit for steady inviscid axisymmetric flow. Solutions of the steady axisymmetric Navier–Stokes equations for vortex breakdown in a pipe sometimes exhibit wavetrains downstream of breakdown (see figure 22 in Beran & Culick 1992). If, as Leibovich (1984) discusses, vortex breakdown is the superposition of a large-amplitude disturbance and smaller-amplitude non-axisymmetric modes resulting from instability, then one possibility is that the measured oscillations are remnants of axisymmetric wavetrains, modified by interaction with the unsteady non-axisymmetric flow.

It is interesting to note that when all the profiles downstream of the disturbance are ensemble averaged to form an estimate of the mean columnar base flow on which the waves are superposed, the wavelength of infinitesimal standing waves computed according to Benjamin's (1962) critical equation (putting $c = 0$ in equation (9.1), below, with $\lambda = 2\pi/\alpha$) is $\lambda/R = 2.0$ for $\beta = 26°$ and $\lambda/R = 0.76$ for $\beta = 29°$. The wall boundary layers were ignored in this calculation; the profiles given by fitting equation (4.3) to the data were extrapolated to a hypothetical pipe wall at a radius equal to the pipe radius less the displacement thickness of the pipe wall boundary layer. Although the assumptions associated with the critical equation are not satisfied by the physical flow (see § 9), correlation with the experimental wavelength is fair, considering the limited number of profiles available to form an approximation of the base flow (three for $\beta = 26°$ and seven for $\beta = 29°$). These results suggest that a more detailed examination of the mean flow structure in the wake of vortex breakdown is necessary. Not only was such a study outside the scope of this paper, but pointwise time-averaged measurements such as those used here are not well-suited to these types of flows (see § 2).

6. Turbulent core flow

For $\beta \geqslant 30°$, the equilibrium position of the spiral disturbance moved upstream, eventually moving into the contraction. Optical access was not available in this part

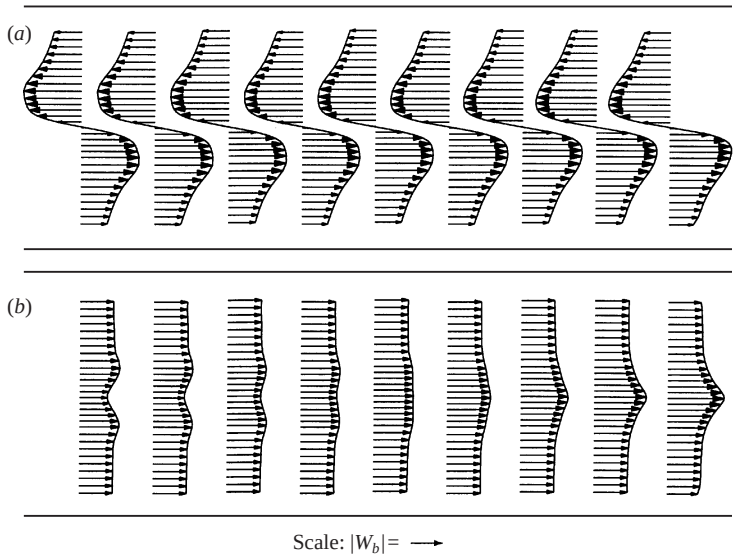

FIGURE 13. (*a*) Azimuthal and (*b*) axial velocity profiles for $\beta = 39°$, $\Omega = 2.05$, $Re = 4934$.

of the apparatus and it was therefore not possible to determine how it continued to develop. Downstream, the dye pattern became increasingly disordered with streamwise distance and increasing β, but remained confined to the core region.

The mean velocity profiles for $\beta = 39°$ are shown in figure 13. At large radii the behaviour is similar to the laminar flow cases, that is, the axial velocity approaches uniformity and the azimuthal velocity approaches a potential vortex. This is consistent with the disturbances being confined to the core region. In the core there is a gradual recovery from wake-like to jet-like axial velocity profiles with streamwise distance, contrasting with the opposite behaviour observed in laminar flow. As a result, the mean flow within the core is convergent and, despite the effects of unsteadiness and viscosity, transport of moment of momentum by the mean flow causes a reduction in the core thickness (as measured by the radial position of maximum azimuthal velocity) with streamwise distance. The slow development of the vortex with streamwise distance seems to suggest that the Reynolds-averaged, quasi-cylindrical approximation should apply. It was not possible to obtain solutions of the quasi-cylindrical equations by neglecting the turbulent terms and using the procedure of Beran & Culick (1992) (as in § 4). On the other hand, the steady laminar axisymmetric viscous solutions obtained by Wang & Rusak (1997*a*) exhibit axial flow acceleration approaching the pipe outlet when the inlet flow is subcritical. Further knowledge of the particular characteristics of turbulence in the current flow are needed if it is to be properly understood. It was not possible to obtain accurate measurements of turbulence due to the limitations described in § 2.

It is interesting to note that the mean circulation distribution develops a logarithmic dependence on radius close to the point of maximum azimuthal velocity $r = r_1$, that is,

$$\frac{\Gamma}{\Gamma_1} = \frac{1}{\kappa} \log_{10} \left(\frac{r}{r_1} \right) + 1, \tag{6.1}$$

where Γ_1 is the circulation at radius r_1. Figure 14(*a*) shows the data from figure 13 re-plotted using log-linear axes. The data collapse onto a single curve for $r/r_1 < 1$.

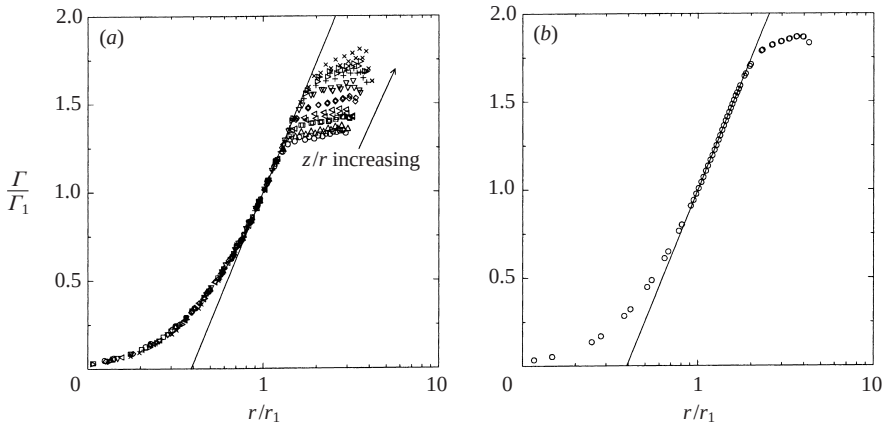

FIGURE 14. Circulation distribution at $\beta = 39°$ for (a) all stations and (b) last station only.

At the first station there is no evidence of logarithmic behaviour but the data subsequently tend to collapse on a line of constant slope in a limited region which increases in extent with streamwise distance. The resolution of the original data was rather coarse in this region, so a finer-resolution traverse was conducted at the last station. These data are shown in figure 14(b) and suggest logarithmic behaviour for $0.9 \lesssim r/r_1 \lesssim 2.0$. The solid line has a slope of $1/\kappa = 2.45$ which is greater than the correct value of $\log_e 10 = 2.303$ necessary to be consistent with the definition of Γ_1 and r_1; however the difference can be explained by errors in estimating r_1 of the order of a few percent. Hoffmann & Joubert (1968) originally noticed logarithmic behaviour in measurements of turbulent trailing vortices and showed that equation (6.1) was consistent with mixing length and similarity arguments analogous to those used in turbulent boundary layers. For the trailing vortex, the vortex sheet roll-up also leads to logarithmic behaviour (Spalart 1998), so turbulence is not the only explanation for that case.

7. Transitional flow II

Between $\beta = 44°$ and $45°$, there was a second abrupt change in flow structure. Unlike vortex breakdown, where transition from one flow state to the other occurred at a particular streamwise station, this second transition was global, affecting the entire flow. Figure 15 shows that the flow at $\beta = 44°$ was qualitatively similar to that at $\beta = 39°$. In contrast, figure 16 shows an annular axial velocity deficit surrounding an axial velocity jet at $\beta = 45°$. This feature, which is absent at $\beta = 44°$, extends right through the working section. The maximum and minimum axial velocity gradually increase in magnitude with streamwise distance. Since $\eta \approx -\partial w/\partial r$, the annular axial velocity deficit means that there is a change in sign of the mean azimuthal vorticity with increasing radius. The mean vortex lines are therefore quite complicated, consisting of left-handed helices surrounding right-handed helices.

Figures 17 and 18 provide a comparison of stream function and circulation for these two flow cases. Isolines of ψ show that the flow close to the centre of the vortex is convergent in both cases; however the annular axial velocity deficit is associated with the development of an external flow divergence. The same trends are evident in the distribution of Γ, although there appears to be some variation in the outer flow near the last station at $\beta = 45°$. Apart from this and other minor variations

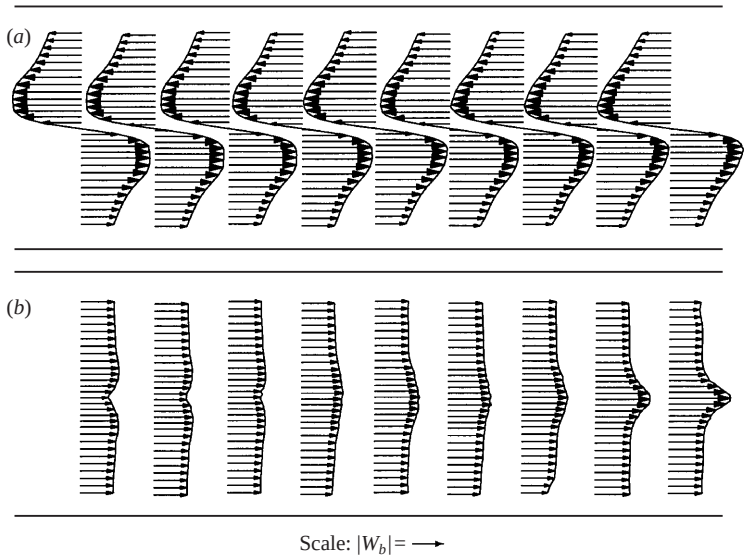

FIGURE 15. (*a*) Azimuthal and (*b*) axial velocity profiles for $\beta = 44°$, $\Omega = 2.56$, $Re = 4906$.

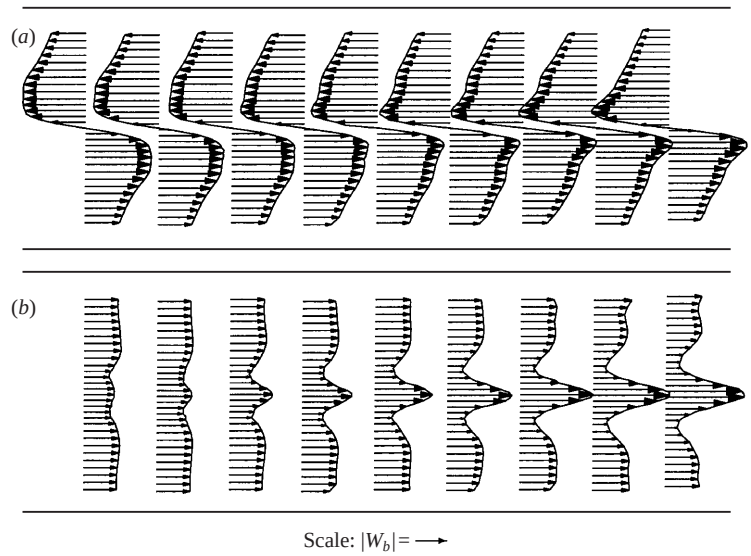

FIGURE 16. (*a*) Azimuthal and (*b*) axial velocity profiles for $\beta = 45°$, $\Omega = 2.68$, $Re = 4915$.

which are discussed below, the outer flow is steady and irrotational. Application of the Bernoulli equation indicates that there is an adverse or positive pressure gradient outside the core. The pressure at the centre of the vortex can then be estimated by assuming the flow to be quasi-cylindrical and integrating

$$\frac{1}{\rho}\frac{\partial P}{\partial r} = \frac{V^2}{r}, \tag{7.1}$$

where ρ is the density and P the mean pressure. These calculations (see Mattner 2000) suggest that the pressure gradient at the centreline is negative.

Careful inspection of figures 15 and 16 reveals isolated departures of the axial

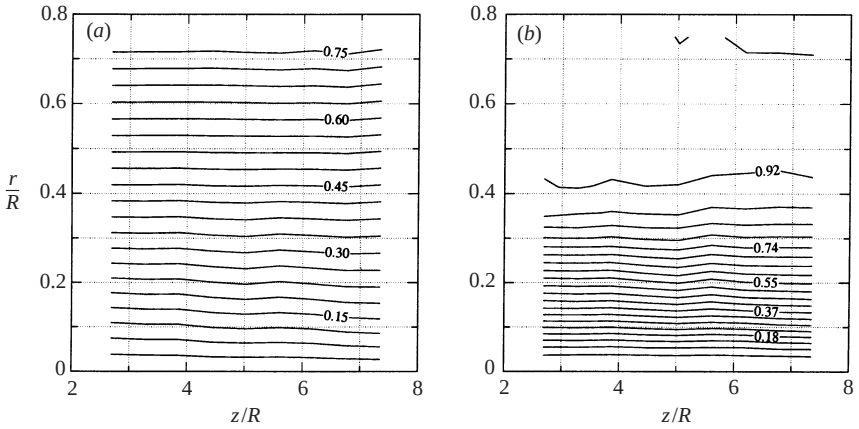

FIGURE 17. Isolines of (*a*) $\langle \psi/\psi_0 \rangle$ and (*b*) $\langle \Gamma/\Gamma_0 \rangle$ for $\beta = 44°$.

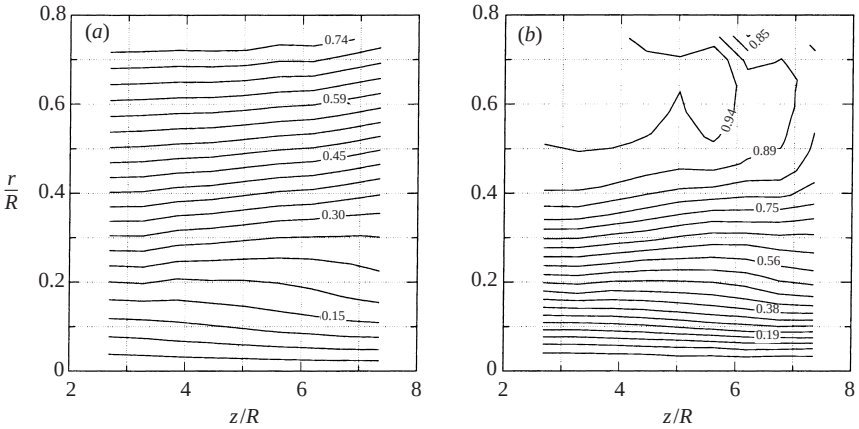

FIGURE 18. Isolines of (*a*) $\langle \psi/\psi_0 \rangle$ and (*b*) $\langle \Gamma/\Gamma_0 \rangle$ for $\beta = 45°$.

velocity from uniformity and axisymmetry close to the walls. Figures 19(*a*) and 19(*b*) show the azimuthal and axial turbulence intensities, $(\overline{v'^2}/W_b^2)^{1/2}$ and $(\overline{w'^2}/W_b^2)^{1/2}$ respectively. Although these data are not considered accurate for the reasons given in § 2, there are isolated turbulent peaks corresponding to the non-uniformities and a general increase in turbulence outside the core near the last station. Unsteadiness explains the circulation variation in the outer flow near the last station at $\beta = 45°$. Flow visualization was conducted by introducing a concentrated dye solution at one azimuthal location upstream of the contraction. Near the end of the working section, helical streaks of dye appeared to lift away from the wall toward the centre of the vortex. A laser sheet was used to obtain a cross-section through these structures and a time sequence is shown in figure 20. The pattern is consistent with two streamwise (in a helical sense since the mean flow is helical) vortical structures of opposite sign lifting away from the wall. The onset of instability occurred further upstream with increasing β until the entire outer flow became unsteady. Escudier *et al.* (1982) observed a series of irregular vortex-ring structures spaced fairly evenly along the length of their jet-driven vortex. They suggested that these were finite-amplitude Taylor–Görtler instabilities distorted by the axial flow and driven by the centrifugal

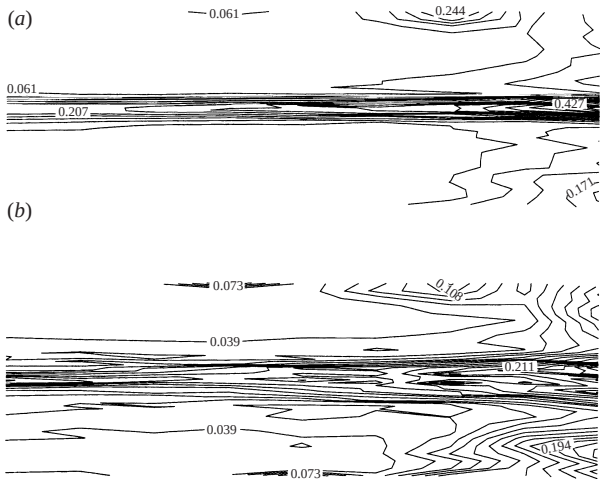

FIGURE 19. (*a*) Azimuthal and (*b*) axial turbulence intensities for $\beta = 45°$, $\Omega = 2.68$, $Re = 4915$.

instability of the pipe wall boundary layer. It was also mentioned that the large-scale mixing in the outer flow might have been unique to their apparatus. The present results indicate that this is not the case.

8. Fully turbulent flow

With further increase in β, the annular axial velocity deficit eventually developed into a region of mean axial flow reversal (regime III). Some difficulty was experienced in obtaining well-converged statistics at swirl intensities in the range $50° \lesssim \beta \lesssim 60°$, possibly due to the transitional nature of the outer flow in this range. Figure 21 shows the mean axial and azimuthal velocity profiles at $\beta = 69°$. The magnitude of the reverse flow is very small in comparison with the peak axial velocity and can barely be detected in these diagrams. Reverse flow is clearly evident from the isolines of ψ in figure 22(*a*). The magnitude of the peak velocities is similar for both components and a factor of eight larger than the bulk axial velocity (note the change in scale from previous diagrams).

The properties of the outer flow are quite different to those for the lower values of β. The axial velocity does not approach uniformity at large radius. Figure 22(*b*) shows that the circulation varies considerably with radius, hence the vortex is far from irrotational. The streamwise variation of Γ does not correlate with that of ψ, hence there is considerable variation of the circulation across stream surfaces. The maximum value of Γ is a factor of three less than that expected from equation (3.4). These effects are consistent with the presence of turbulence in the outer flow. Escudier *et al.* (1982) also observed radial variation of the circulation with unsteady outer flow and suggested that the core acted as a source of vorticity which was mixed uniformly through the outer region by turbulence. Mixing of negative vorticity from the wall region with positive vorticity from the core in the intermediate region might explain the large reduction in the maximum circulation.

9. Discussion

These experiments reveal a complex transition process as Ω is increased with Re fixed at 4900. Like all previous studies, regime III was found to exist only at very

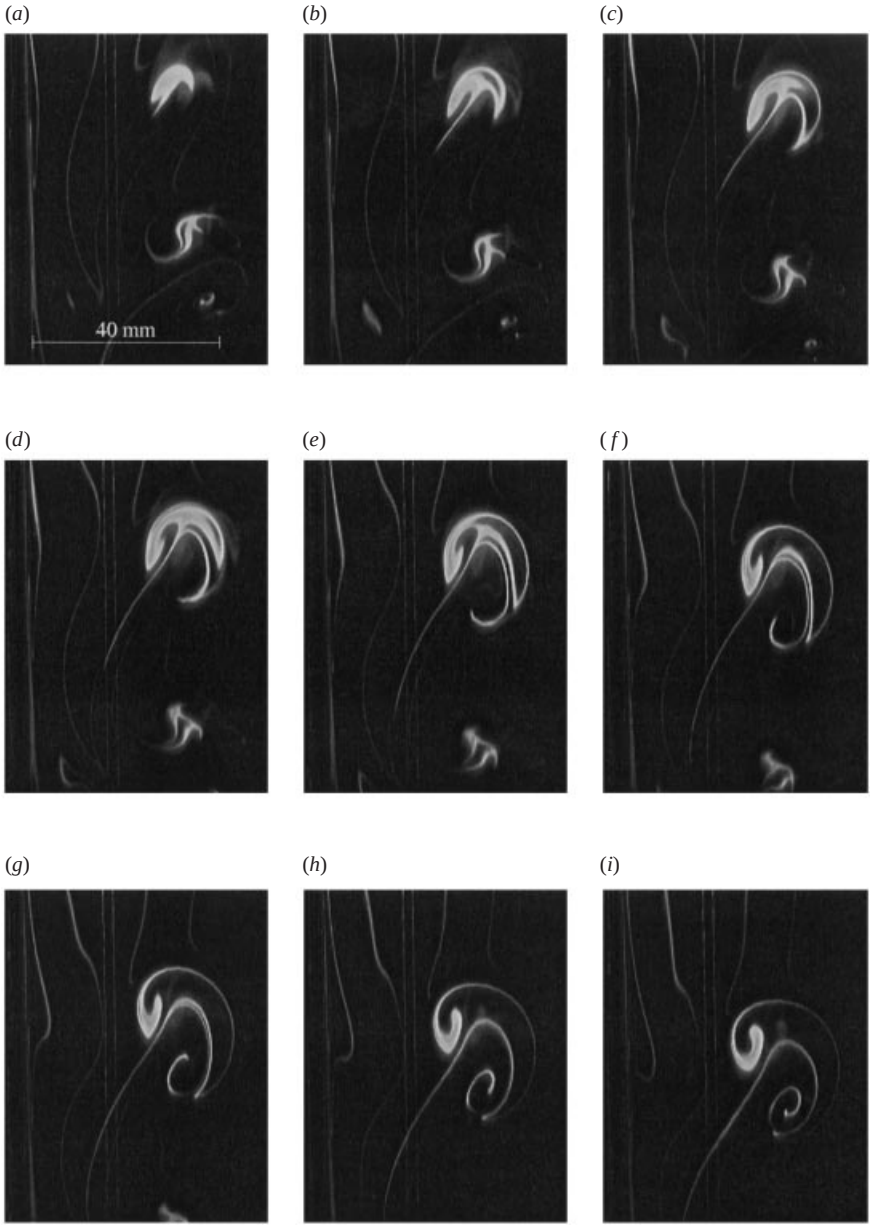

FIGURE 20. Instability near $z/R \approx 7.34$ for $\beta = 44°$, $Re = 4050$. Flow is from top to bottom with the pipe wall near the left of each frame. (*a*) $\Delta t = 0$ s, (*b*) 0.2 s, (*c*) 0.4 s, (*d*) 0.6 s, (*e*) 0.8 s, (*f*) 1.0 s, (*g*) 1.2 s, (*h*) 1.4 s, (*i*) 1.6 s

high swirl intensity. Previous measurements of regime III in a jet-driven version of the apparatus used in this study (Mattner 2000) are qualitatively similar to those in figure 21. This suggests that details of the upstream boundary conditions are relatively unimportant.

Previous studies of regime III do not make explicit reference to vortex breakdown. Regime II is consistent with the post-breakdown behaviour observed by both Harvey (1962) and Escudier & Keller (1985) and it is possible that vortex breakdown was

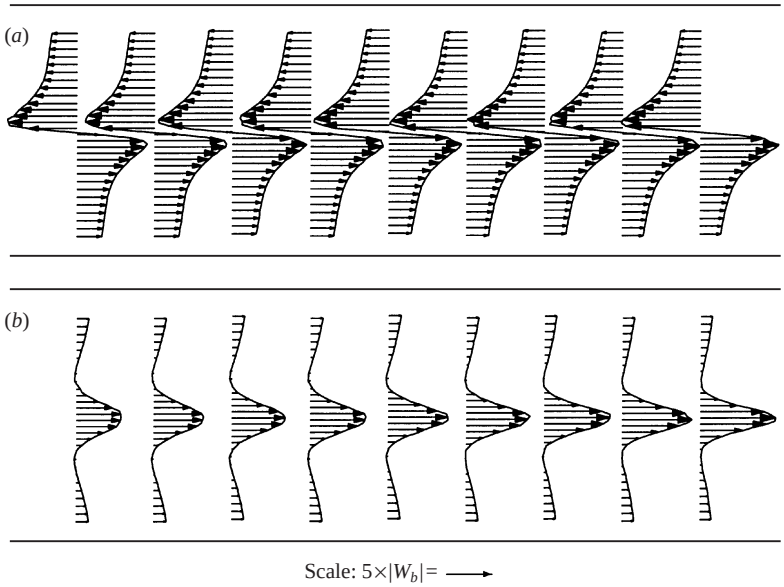

FIGURE 21. (*a*) Azimuthal and (*b*) axial velocity profiles for $\beta = 69°$, $\Omega = 21.5$, $Re = 4953$.

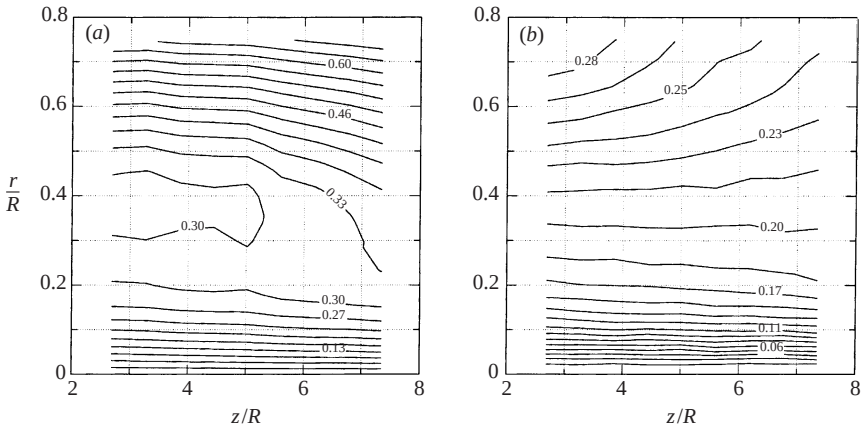

FIGURE 22. Isolines of (*a*) $\langle \psi/\psi_0 \rangle$ and (*b*) $\langle \Gamma/\Gamma_0 \rangle$ for $\beta = 69°$.

associated with regime II flow in Nuttal's (1953) original experiment. In the present experiments, vortex breakdown occurred without mean axial flow reversal. Thus, although regime II was not observed, the transition process may have been essentially equivalent to the three-stage process originally reported by Nuttal (1953). Mattner *et al.* (1996) did not observe vortex breakdown in the jet-driven vortex. That flow suffered from very high turbulence intensity and asymmetry and it therefore seems possible that excessive unsteadiness or asymmetry sometimes prevents its identification or formation.

Various criteria have been proposed to predict vortex breakdown. Figure 23(*a*) shows the maximum helix angle $\gamma_{max} = \max[\tan^{-1}(v/w)]$ as a function of streamwise distance. Vortex breakdown is expected when $\gamma_{max} \geqslant \gamma_c \approx 50°$ (Delery 1994). Figure 23(*b*) shows the Rossby number $Ro = w_1/r_1\omega$ introduced by Spall, Gatski & Grosch (1987), where w_1 is the axial velocity at the radial position of maximum

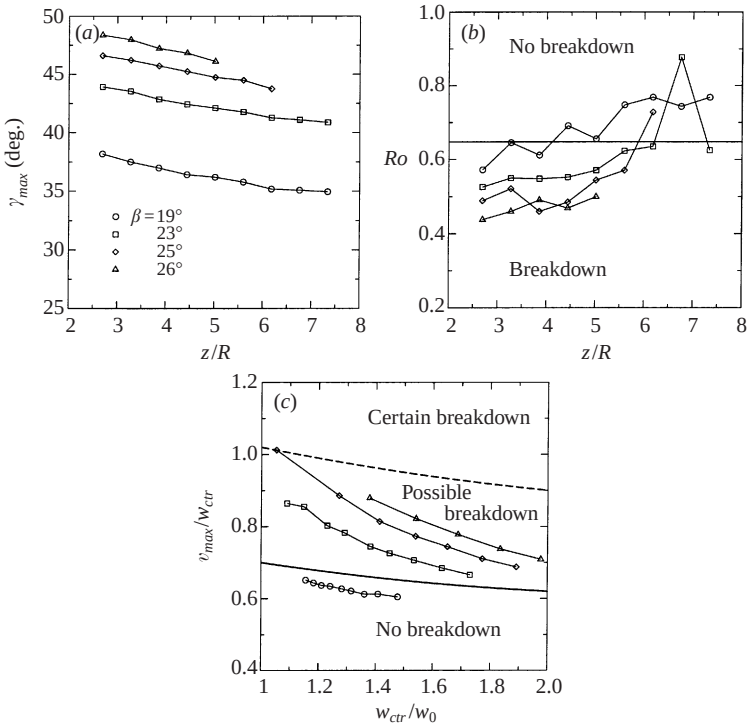

FIGURE 23. Evaluation of three vortex breakdown criteria: (*a*) γ_{max}, (*b*) *Ro* and (*c*) v_{max}/w_{ctr}. The key in (*a*) applies to all three plots. Vortex breakdown occurred for $\beta = 25°$ and 26° (29° has been omitted). Values downstream of vortex breakdown have been omitted. In (*c*), the solid line corresponds to $(v_{max}/w_{ctr})_0$ and the dashed line to $(v_{max}/w_{ctr})_1$ for a Q-vortex with $r_1/R = 0.198$ (from figure 4*b*, Rusak *et al.* 1998).

azimuthal velocity r_1 and $\omega = \mathrm{d}v/\mathrm{d}r$ at $r = 0$. Vortex breakdown is expected when $Ro < Ro_c$ where Ro_c is an empirically determined, Reynolds number dependent parameter. For core Reynolds numbers $Re_{core} = w_1 r_1/\nu > 100$ (for $19° \leqslant \beta \leqslant 29°$, $430 < Re_{core} < 630$), $Ro_c \approx 0.65$. Figure 23(*c*) shows the parameter v_{max}/w_{ctr} introduced by Rusak, Whiting & Wang (1998*b*), where v_{max} is the maximum azimuthal velocity and w_{ctr} is the axial velocity at the axis of symmetry. There are two critical values $(v_{max}/w_{ctr})_0$ and $(v_{max}/w_{ctr})_1$ which follow from the rigorous theoretical study of inviscid axisymmetric vortex breakdown by Wang & Rusak (1996*a*, *b*, 1997*b*). For $v_{max}/w_{ctr} < (v_{max}/w_{ctr})_0$, only one steady-state solution is possible, which is columnar. For $(v_{max}/w_{ctr})_0 < v_{max}/w_{ctr} < (v_{max}/w_{ctr})_1$, two steady-state solutions may develop, depending on the initial disturbances to the base flow. One of these is columnar, the other describes flow past an elongated stagnation zone. For $v_{max}/w_{ctr} > (v_{max}/w_{ctr})_1$, the flow always develops a stagnation zone. For the Q-vortex, these critical values depend on the vortex core thickness r_1/R and the ratio w_{ctr}/w_0 where w_0 is the uniform axial velocity at large radius. For $\beta \leqslant 29°$, the core thickness varies with streamwise distance, taking values in the range $0.15 < r_1/R < 0.23$ upstream of vortex breakdown. The average value of $r_1/R = 0.19$ corresponds closely to figure 4*b* from Rusak *et al.* (1998*b*), hence the critical values have been extracted from that figure.

These plots illustrate the ambiguity of applying simple criteria to viscous vortex flows, at least at the current Reynolds number. If attention is focused on a single axial station, all the criteria approach more critical values with increasing swirl; however

it is not clear which axial station should be used as a reference. The maximum helix angle (figure 23*a*) decreases with streamwise distance, erroneously suggesting that the vortex is less likely to break down. The Rossby number criterion (figure 23*b*) incorrectly predicts vortex breakdown for the two quasi-cylindrical cases, $\beta = 19^\circ$ and $\beta = 23^\circ$. The scatter highlights the sensitivity of the result to the estimate of the gradient ω. The parameter v_{max}/w_{ctr} (figure 23*c*) performs better than γ_{max} and Ro, correctly predicting the absence of vortex breakdown for $\beta = 19^\circ$ and the possibility of vortex breakdown for $\beta = 25^\circ$ and 26°. Although breakdown did not occur for $\beta = 23^\circ$, this is not inconsistent with the theory, which only predicts the possibility of breakdown for this case. If breakdown had occurred (the transients associated with starting the apparatus are extremely large), it would have been located downstream of the working section and therefore close to the orifice. Wang & Rusak (1996*a*, *b*, 1997*b*) use a boundary condition which is not compatible with the converging flow close to an orifice. On the other hand, it is possible that had profiles been available further upstream, these might have explicitly predicted the absence of vortex breakdown.

Escudier & Keller's (1985) results suggest that downstream boundary conditions have strong upstream effects when the flow is subcritical. They used the maximum flow helix angle γ_{max} as a diagnostic to help determine the flow state. When γ_{max} exceeded that of a critical reference vortex (a Rankine vortex), the flow was considered subcritical. This method assumes that the actual flow is approximated well by the chosen reference vortex. The flow state can be determined directly by solving the eigenvalue problem

$$\phi_{yy} - \left[\frac{\alpha^2}{2y} + \frac{W_{yy}}{W-c} - \frac{I_y}{2y^2(W-c)^2}\right]\phi = 0 \tag{9.1}$$

for the maximum and minimum wave speeds c_+ and c_- (Benjamin 1962). Note that $y = r^2/2$, $I = yV^2$, $\phi(y)$ is the disturbance stream function, c the wave speed, α the wavenumber and subscripts denote differentiation, that is,

$$\phi_{yy} = \frac{\mathrm{d}^2\phi}{\mathrm{d}y^2}, \quad W_{yy} = \frac{\mathrm{d}^2 W}{\mathrm{d}y^2} \quad \text{and} \quad I_y = \frac{\mathrm{d}I}{\mathrm{d}y}.$$

The maximum and minimum wave speeds are always associated with extremely long waves and it is therefore possible to take the limit $\alpha \to 0$ when calculating c_+ and c_-. When the Froude-like number introduced by Benjamin,

$$N = \frac{c_+ + c_-}{c_+ - c_-}, \tag{9.2}$$

is greater than 1, the flow is supercritical; when less than 1 it is subcritical. In the context of wave propagation, the critical equation is derived from a perturbation analysis of a steady columnar axisymmetric flow. The results are not valid when there are large streamwise gradients (e.g. near vortex breakdown). The infinite-wavelength limit is not appropriate in a finite-length apparatus. For sufficiently long waves, the gradual streamwise development of the vortex due to viscosity (as observed in figures 4 and 11) will eventually become important. The presence of turbulence in the vortex breakdown wake introduces further uncertainties. Escudier & Keller (1985) suggest that knowledge of the flow state is a fundamental element in understanding the difference in behaviour of the slightly swirled and highly swirled flows. $N(z)$ was therefore computed (for full details, see Mattner 2000) for flows up to $\beta = 39^\circ$ and the results are shown in figure 24. The value of $N(z)$ corresponds to that of an hypothetical steady columnar axisymmetric flow with velocity profiles from the axial

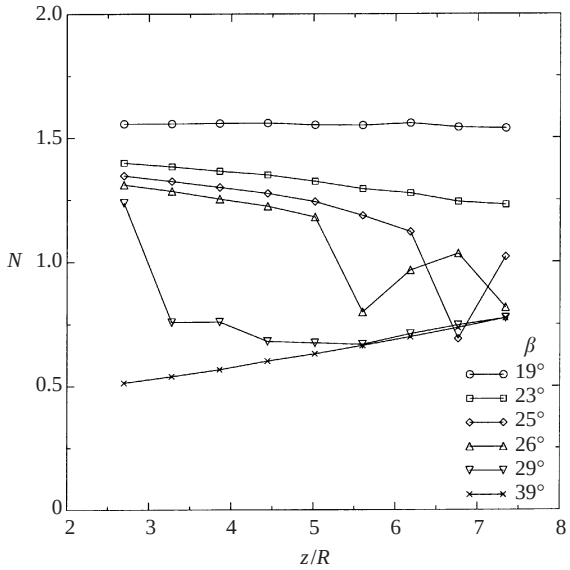

FIGURE 24. Benjamin's (1962) classification of flow state for $\beta \leqslant 39°$.

station z. If it is assumed that the properties of this hypothetical flow are reflected in the physical flow, figure 24 suggests that prior to vortex breakdown the flow was supercritical and gradually approached the critical condition with streamwise distance. Vortex breakdown occurred when the flow was still slightly supercritical ($N \approx 1.2$) and was associated with a transition from supercritical to subcritical flow. This result is consistent with Benjamin's (1962) theory, as well as other experimental results (Leibovich 1984). For $\beta = 39°$, the subcritical post-breakdown flow recovered toward the critical condition with streamwise distance.

For supercritical flow, Escudier & Keller (1985) point out that the influence of a contraction on the upstream flow consists of a global increase in pressure and a local acceleration close to the exit. The features of the pre-breakdown flow are therefore determined by upstream boundary conditions. Thus the flow behaviour described in § 4 is similar to other accounts of vortex flow in guide vane apparatus (i.e. similar upstream boundary conditions). Furthermore, it is possible to accurately compute the flow with the quasi-cylindrical equations using upstream information alone.

The post-breakdown mean flow was subcritical and may therefore have been sensitive to downstream boundary conditions as described by Escudier & Keller (1985). In their experiments, the absence of mean axial flow reversal on the axis following vortex breakdown was associated with either the subcritical post-breakdown flow becoming supercritical upstream of the outlet, or with the effect of a contraction on a flow which remains subcritical. In the latter case, a strong (79% area) contraction produced a flow with an annular axial velocity deficit and a central jet, qualitatively similar to the present flow at $\beta = 45°$. For $\beta \leqslant 44°$ the present flow is unidirectional and approaches the critical condition with streamwise distance, but there is no evidence of an annular axial velocity deficit despite the presence of a severe (97% area) contraction at $z/R = 10.48$ (i.e. the orifice). If these results are to be consistent with Escudier & Keller (1985), then they suggest the flow becomes supercritical upstream of the outlet for $\beta \leqslant 44°$. At $\beta = 45°$ the flow remains subcritical and the contraction causes an annular axial velocity deficit to develop far upstream. It was

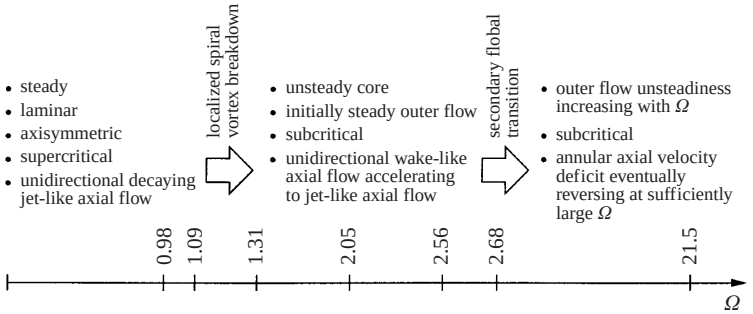

FIGURE 25. Outline of transition to regime III flow.

not possible to test this hypothesis because the orifice outlet was outside the range of the traverse. Such a study would be complicated because the axial gradients are not small in the vicinity of the outlet hence equation (9.1) could not be used to determine the flow state in that region.

Even if the above scenario proves correct, it would still not provide a specific explanation of the annular axial velocity deficit or reversal. This requires a detailed understanding of the interaction between the downstream boundary conditions and the upstream flow. A related interaction was modelled by Rosenzweig, Lewellen & Ross (1964) for a bath tub vortex, where swirling flow enters radially and exhausts axially through an orifice. For the interior flow, they used the high-swirl asymptotic solution of Lewellen (1962) which applies to steady axisymmetric viscous flow. In this solution, the lowest-order term of the circulation is independent of axial distance and the lowest-order term of the stream function varies linearly between its boundary values, hence the endwall boundary layer and geometry exert a considerable upstream effect. By coupling this solution with a separate boundary layer analysis, it was possible to obtain radial and axial flow reversals. Note that this geometry is different to the one studied in this paper, but may be relevant in some limited vicinity of the outlet orifice. Although it is possible to extend Lewellen's (1962) asymptotic solution to flows with significant axial flow, the main difficulty is then related to the additional effects of turbulence in both the core and outer flow in the highly swirled regimes in which it is valid.

10. Conclusion

A complex transition process from regime I to regime III was observed as the swirl intensity was increased with *Re* fixed at 4900. The main features are summarized in figure 25. This exploratory study has highlighted several areas in need of further investigation, including the unsteady non-axisymmetric vortex breakdown wake, the turbulent structure of the post-breakdown flows and transition to turbulence in the outer flow. In particular, a physical explanation of the transition to annular axial flow deficit and reversal (regime III) remains outstanding. A complete understanding of the flow must take into account the effects of unsteadiness in the core and outer flow and the interaction between upstream and downstream boundary conditions.

For $\beta \leqslant 23^\circ$, the flow is consistent with other guide-vane-driven flows commonly encountered in the literature. It is not strongly affected by downstream boundary conditions. It is therefore expected that (for $\beta \leqslant 23^\circ$) results of the subsequent study of vortex flow past a sphere (Mattner *et al.* 2002) will not be unique to our apparatus. The present data serve as a reference from which the additional effects of the sphere may be determined.

This work was funded through the Australian Research Council and their support is gratefully acknowledged.

REFERENCES

Althaus, W., Brucker, C. H. & Weimer, M. 1995 Breakdown of slender vortices. In *Fluid Vortices* (ed. S. I. Green), pp. 373–426. Kluwer.

Benjamin, T. B. 1962 Theory of the vortex breakdown phenomena. *J. Fluid Mech.* **14**, 593–629.

Benjamin, T. B. 1967 Some developments in the theory of vortex breakdown. *J. Fluid Mech.* **28**, 65–84.

Beran, P. S. & Culick, F. E. C. 1992 The role of non-uniqueness in the development of vortex breakdown in tubes. *J. Fluid Mech.* **242**, 491–527.

Binnie, A. M. 1957 Experiments on the slow swirling flow of a viscous liquid through a tube. *Q. J. Mech. Appl. Maths* **3**, 276–290.

Boutier, A. 1985 Laser velocimetry and wall approach limitations. In *Intl Symp. on Laser Anemometry* (ed. A. Dybbs & P. A. Pfund). FED vol. 33, pp. 75–82. ASME.

Brown, G. L. & Lopez, J. M. 1990 Axisymmetric vortex breakdown. Part 2. Physical mechanisms. *J. Fluid Mech.* **221**, 553–576.

Brücker, C. 1993 Study of vortex breakdown by particle tracking velocimetry (PTV). Part 2: Spiral-type vortex breakdown. *Exps. Fluids* **14**, 133–139.

Brücker, C. & Althaus, W. 1995 Study of vortex breakdown by particle tracking velocimetry (PTV). Part 3: Time-dependent structure and development of breakdown-modes. *Exps. Fluids* **18**, 174–186.

Delery, J. M. 1994 Aspects of vortex breakdown. *Prog. Aerospace Sci.* **30**, 1–59.

Devenport, W. J., Rife, M. C., Liapis, S. I. & Follin, G. J. 1996 The structure and development of a wing-tip vortex. *J. Fluid Mech.* **312**, 67–106.

Donaldson, C. & Sullivan, R. D. 1960 Behavior of solutions of the Navier–Stokes equations for a complete class of three-dimensional viscous vortices. In *Proc. 1960 Heat Transfer and Fluid Mechanics Institute* (ed. D. M. Mason, W. C. Reynolds & W. G. Vincenti), pp. 16–26. Stanford University Press.

Drain, L. E. 1980 *The Laser Doppler Technique*. John Wiley & Sons.

Escudier, M. P. 1988 Vortex breakdown: Observations and explanations. *Prog. Aerospace Sci.* **25**, 185–229.

Escudier, M. P., Bornstein, J. & Maxworthy, T. 1982 The dynamics of confined vortices. *Proc. R. Soc. Lond.* A **382**, 335–360.

Escudier, M. P. & Keller, J. J. 1985 Recirculation in swirling flow: A manifestation of vortex breakdown. *AIAA J.* **23**, 111–116.

Faler, J. H. & Leibovich, S. 1977 Disrupted states of vortex flow and vortex breakdown. *Phys. Fluids* **20**, 1385–1400.

Faler, J. H. & Leibovich, S. 1978 An experimental map of the internal structure of a vortex breakdown. *J. Fluid Mech.* **86**, 313–335.

Garg, A. K. & Leibovich, S. 1979 Spectral characteristics of vortex breakdown flowfields. *Phys. Fluids* **22**, 2053–2064.

Guo, Z. & Dhir, V. K. 1990 Flow reversal in injection induced swirl flow. *Single and Multiphase Convective Heat Transfer* **145**, 23–30.

Hall, M. G. 1966 The structure of concentrated vortex cores. *Prog. Aerospace Sci.* **7**, 53–110.

Hall, M. G. 1967 A new approach to vortex breakdown. In *Proc. 1967 Heat Transfer and Fluid Mechanics Institute* (ed. P. A. Libby, D. B. Olfe & C. W. Van Atta), pp. 319–340. Stanford University Press.

Harvey, J. K. 1962 Some observations of the vortex breakdown phenomena. *J. Fluid Mech.* **14**, 585–592.

Hoffmann, E. R. & Joubert, P. N. 1963 Turbulent line vortices. *J. Fluid Mech.* **16**, 395–411.

Kribus, A. & Leibovich, S. 1994 Instability of strongly nonlinear waves in vortex flows. *J. Fluid Mech.* **269**, 247–264.

Leibovich, S. 1970 Weakly nonlinear waves in rotating fluids. *J. Fluid Mech.* **42**, 803–822.

Leibovich, S. 1978 The structure of vortex breakdown. *Annu. Rev. Fluid Mech.* **10**, 221–246.

Leibovich, S. 1984 Vortex stability and breakdown: Survey and extension. *AIAA J.* **22**, 1192–1206.

Leibovich, S. & Kribus, A. 1990 Large-amplitude wavetrains and solitary waves in vortices. *J. Fluid Mech.* **216**, 459–504.

Lewellen, W. S. 1962 A solution for three-dimensional vortex flows with strong circulation. *J. Fluid Mech.* **14**, 420–432.

Lopez, J. M. 1994 On the bifurcation structure of axisymmetric vortex breakdown in a constricted pipe. *Phys. Fluids* **6**, 3683–3693.

Mattner, T. W. 2000 Vortical flow past a sphere. PhD Thesis. University of Melbourne.

Mattner, T. W., Joubert, P. N. & Chong, M. S. 1996 Investigation of the effect of downstream boundary conditions on a confined vortex flow. In *First Australian Conf. on Laser Diagnostics in Fluid Mechanics and Combustion* (ed. A. R. Masri & D. R. Honnery), pp. 180–185. University of Sydney.

Mattner, T. W., Joubert, P. N. & Chong, M. S. 2002 Vortical flow. Part 2. Flow past a sphere in a constant diameter pipe. In preparation.

Nissan, A. H. & Bresan, V. P. 1961 Swirling flow in cylinders. *AIChE J.* **7**, 543–446.

Nuttal, J. 1953 Axial flow in a vortex. *Nature* **172**, 582.

Patrick, W. P. 1985 Error analysis for benchmark fluid dynamic experiments. Part 1: Error analysis methodology and the quantification of laser velocimeter error sources. *United Technologies Research Centre Tech. Rep.* R85-151772.

Rosenzweig, M. L., Lewellen, W. S. & Ross, D. H. 1964 Confined vortex flows with boundary-layer interaction. *AIAA J.* **2**, 2127–2134.

Rusak, Z., Wang, S. & Whiting, C. H. 1998*a* The evolution of a perturbed vortex in a pipe to axisymmetric vortex breakdown. *J. Fluid Mech.* **366**, 211–237.

Rusak, Z., Whiting, C. H., & Wang, S. 1998*b* Axisymmetric breakdown of a Q-vortex in a pipe. *AIAA J.* **36**, 1848–1853.

Sarpkaya, T. 1971 On stationary and travelling vortex breakdown. *J. Fluid Mech.* **45**, 545–559.

Snyder, D. E. & Spall, R. E. 2000 Numerical simulation of bubble-type vortex breakdown within a tube-and-vane apparatus. *Phys. Fluids* **12**, 603–608.

Spalart, P. R. 1998 Airplane trailing vortices. *Annu. Rev. Fluid Mech.* **30**, 107–138.

Spall, R. E., Gatski, T. B. & Grosch, C. E. 1987 A criterion for vortex breakdown. *Phys. Fluids* **30**, 3434–3440.

Uchida, S., Nakamura, Y. & Oshawa, M. 1985 Experiments on the axisymmetric vortex breakdown in a swirling air flow *Trans. Japan Soc. Aero. Space Sci.* **27**, 206–216.

Uchida, S., Nakamura, Y., Zhang, J. Z. & Sagawa, N. 1987 An experiment on a spiral type of vortex breakdown of a swirling flow in a pipe. *Trans. Japan Soc. Aero. Space Sci.* **30**, 38–44.

Vakili, A. D., Tennent, S. G. & Panchapakesan, N. R. 1996 An experimental study of confined multi-cell vortex flows. *Tech. Rep.* 96-0806. AIAA.

Wang, S. & Rusak, Z. 1996*a* On the stability of an axisymmetric rotating flow in a pipe. *Phys. Fluids* **8**, 1007–1016.

Wang, S. & Rusak, Z. 1996*b* On the stability of non-columnar swirling flows. *Phys. Fluids* **8**, 1017–1023.

Wang, S. & Rusak, Z. 1997*a* The effect of slight viscosity on a near-critical swirling flow in a pipe. *Phys. Fluids* **9**, 1914–1927.

Wang, S. & Rusak, Z. 1997*b* The dynamics of a swirling flow in a pipe and transition to axisymmetric vortex breakdown. *J. Fluid Mech.* **340**, 177–223.

Winter, A. R., Graham, L. J. W. & Bremhorst, K. 1991*a* Effects of time scales on velocity bias in LDA measurements using sample and hold processing. *Exps. Fluids* **11**, 147–152.

Winter, A. R., Graham, L. J. W. & Bremhorst, K. 1991*b* Velocity bias associated with laser Doppler anemometer controlled processors. *Trans. ASME: J. Fluids Engng* **113**, 250–255.